

Space reconstruction of the morphology and kinematics of axisymmetric radio sources

P.N. Diep^{*}, N.T. Phuong, D.T. Hoai, P.T. Nhung, N.T. Thao, P. Tuan-Anh and P. Darriulat

Department of Astrophysics, Vietnam National Satellite Center (VNSC), Vietnam Academy of Science and Technology (VAST), 18 Hoang Quoc Viet, Ha Noi, Viet Nam

Accepted XXX. Received YYY; in original form ZZZ

ABSTRACT

The unprecedented quality of the observations available from the Atacama Large Millimetre/sub-millimetre Array (ALMA) calls for analysis methods making the best of them. Reconstructing in space the morphology and kinematics of radio sources is an underdetermined problem that requires imposing additional constraints for its solution. The hypothesis of rotational invariance, which is a good approximation to, or at least a good reference for the description of the gas envelopes of many evolved stars and protostars, is particularly efficient in this role. In the first part of the article, a systematic use of simulated observations allows for identifying the main problems and for constructing quantities aimed at solving them. In particular the evaluation of the orientation of the star axis in space and the differentiation between expansion along the star axis and rotation about it are given special attention. The use of polar rather than Cartesian sky coordinates to display the results of the analysis is shown to often better match the morphology and kinematics of actual stars. The radial dependence of the gas density and temperature and the possible presence of velocity gradients are briefly considered. In the second part, these results are applied to a few stars taken as examples with the aim of evaluating their usefulness when applied to concrete cases. A third part takes stock of what precedes and formulates some guidelines for modelling the radio emission of axisymmetric radio sources, limited however to the mathematics and geometry of the problem, physics considerations being generally ignored.

Key words: stars: late-type – stars: circumstellar matter – stars: kinematics and dynamics – stars: winds, outflows – stars: protostars – radio lines: stars

1 INTRODUCTION

From the end of their lifetime on the Main Sequence to their death as White Dwarfs, most stars evolve from a perfectly spherically symmetric morphology to the often very irregular shapes of Planetary Nebulae dissolving into the Interstellar Medium (ISM). The transition, with Red Giant and Asymptotic Giant Branch (AGB) as main intermediate states, is the object of intense study. The first departure from spherical symmetry is often observed to be the appearance of a bipolar outflow, axisymmetry – meaning invariance by rotation (rather than symmetry) about an axis – replacing spherical symmetry. Many observations, whether of the dust from infrared, mid-infrared and far-infrared or of the gas from atomic radio or molecular millimetre/sub-millimetre emission, in particular from carbon monoxide, are

interpreted in terms of such symmetry. Namely they aim at giving a model of the circumstellar envelope (CSE) displaying invariance with respect to rotation about a well-defined star axis, averaging over deviations from it, assumed to be small. The physics mechanisms at play in such symmetry breaking are not well understood and many observations aim at their clarification. The presence of a companion accreting gas from the dying star is very often invoked, but the roles of rotation and of magnetic field – how the angular momentum and magnetic flux of the original star are distributed between the degenerate core and the CSE – are still unclear.

The study of protostars displays striking similarities with the study of evolved stars. The CSE is now in-falling rather than expanding but axisymmetry is again found to be a good working approximation in many cases and the mechanisms that govern the transition from gravitational in-fall

^{*} E-mail: pndiep@mail.vnsc.org.vn

to formation of a rotating disk, accretion by the protostar and emission of a bipolar outflow are still partly unclear.

In the present article, we focus on the millimetre/sub-millimetre observation of the expanding CSE of AGB stars, typically from carbon monoxide emission, but many developments apply as well to the in-falling CSEs of protostars.

The data are in the form of flux densities f , measured in Jansky/beam in bins (pixels) of sky coordinates (y to the east and z to the north) and of frequency, the latter being expressed in terms of the Doppler velocity V_x measured along the line of sight taken as x axis. Making a model of the CSE from such observations can be conceptually separated in two steps, even if, in practice, they are generally mixed: the reconstruction in space of the gas properties, a purely mathematical problem, and the conception of a physical model accounting for the distribution in space of the gas density, temperature and velocity.

The former, the mathematical problem, is what is addressed here. It aims at measuring, at each point of space coordinates (x, y, z) , the temperature T , density d and velocity vector (V_x, V_y, V_z) of the gas. This means, for each (y, z) pixel, to calculate the values taken by T , d and the three velocity components as a function of x . While the assumption of rotational invariance about the star axis brings a helpful constraint, the problem is obviously unsolvable without making additional hypotheses (six unknowns in each pixel, x , T , d and the components of the velocity vector, for only two input data: the measured flux density $f(y, z, V_x)$ and the Doppler velocity V_x). From the beginning, we simplify the density and temperature side of the problem by introducing an effective emissivity ρ (in earlier publications we called it effective density, which is improper), defined as

$$\rho(x, y, z) = f(y, z, V_x) dV_x / dx \quad (1)$$

implying

$$\int f(y, z, V_x) dV_x = \int \rho(x, y, z) dx = F(y, z) \quad (2)$$

The effective emissivity is therefore a function of the gas density, the abundance of the emitting gas, the population of the emitting quantum state and the probabilities of emission and absorption of the detected radiation. It is equal to the volume emissivity in the optically thin limit. In general, we measure all distances as angular distances, including along the line of sight: an angular distance of $1''$ means a distance of 1 AU times the distance of the star from the Earth measured in parsec, the effective emissivity being measured in $\text{Jy km s}^{-1} \text{arcsec}^{-3}$. Also from the beginning, we often restrict our considerations to centrally symmetric star morphologies and kinematics, implying $f(y, z, V_x) = f(-y, -z, -V_x)$.

The problem of reconstructing CSE properties in space from radio observations is not new and has been addressed for decades by radio astronomers. What is new, however, is the availability of observations of unprecedented spatial and spectral resolution in the millimetre and sub-millimetre ranges, with the recent operation of the ALMA interferometer. It opens a new era in millimetre and sub-millimetre radio astronomy and requires analysis methods that make the best of the excellent quality of the data that it provides, namely allowing for more quantitative conclusions to be reliably drawn from observations than was previously possible.

Indeed, the sensitivity and spatial resolution that could be reached before ALMA were such that one had often to be satisfied with qualitative statements obtained from the visual inspection of channel maps, spectral maps and position-velocity (P-V) diagrams. In particular, the reliability and uniqueness of the proposed models could rarely be quantitatively discussed.

The general problem of reconstructing (one says “deprojecting”) a 3-D image from its 2-D projection is a topic of broad interest and the subject of abundant literature (see for example [Ihrke et al. 2008](#)). It has been addressed with particular attention in the domain of optical astronomy, often with emphasis on providing tools that can be used, interactively if possible, by a broad community of people having little expertise in programming, not only for research applications but also for educational purposes, planetarium simulations, etc... An archetype of such 3-D modelling tool is the SHAPE software of [Steffen et al. \(2011\)](#) which makes optimal use of state of the art knowledge in computer visualisation and obtains excellent results in terms of accuracy and computer time.

As the problem is obviously underdetermined (it boils down to solving integral equation 2) additional hypotheses need to be made. Axisymmetry is the most common ([Leahy 1991](#); [Palmer 1994](#), [Magnor et al. 2004 & 2005](#)). In this case, deprojection is relatively straightforward once the orientation of the symmetry axis in space is known. But, while the projection of the symmetry axis on the sky plane is directly revealed, its inclination with respect to the line of sight is more hidden and its evaluation requires algorithms such as chi square minimization and/or iterative approximations and may result in significant uncertainties. An interesting approach has been explored by [Lintu et al. \(2007\)](#) in the case of the circumstellar dust of Planetary Nebulae illuminated by the central star. They do not assume any symmetry but make use of the properties of the scattered light to obtain a plausible approximation of the dust distribution.

Most of the literature, however, concentrates on the morphology deprojection without considering the kinematic deprojection. Morphology deprojection is from 2-D on the sky plane to 3-D in space. Kinematic deprojection implies, in addition, going from the 1-D Doppler velocity to the 3-D space velocity, or, equivalently, from the 3-D datacube (2-D on the sky plane + 1-D for the Doppler velocity) to the 6-D phase space (3-D for space coordinates and 3-D for velocity coordinates). Kinematic deprojection is therefore even more underdetermined than morphology deprojection. A notable exception is from [Sabbadin \(1984\)](#) and [Sabbadin et al. \(2000\)](#) who evaluate the velocity field under the assumption of radial expansion. The SHAPE software also allows for including kinematic considerations but the accent is on morphology more than on kinematics: it inherits from optical observations, where the measurement of velocities is difficult, requiring methods such as long-slit spectroscopy, while in radio astronomy the full velocity spectrum is directly available in each pixel. Yet, the flexibility of the code makes it possible to produce simulations including arbitrary velocity fields, such as was done recently by [Decin et al. \(2015\)](#) using ALMA data.

In comparison with the existing literature, the present paper displays both similarities and differences. The similarities are very general and include the type of problems one is

facing, the considerations that they inspire and the analysis of how they should be approached.

The differences result in part from the restriction of our work to the case of evolved stars and protostars observed in millimetre and sub-millimetre astronomy. In this domain, the information carried by kinematics is usually richer than that carried by morphology. This is due both to the power of the instrument in providing simply accurate velocity spectra and in the physics of evolved stars, with a morphology departing rather late from spherical while important winds can be already revealed in an early phase of their evolution. Much of the existing literature on optical deprojection addresses the case of Planetary Nebulae, with morphologies of often extreme complexity. This is not the case for evolved stars; even in the case of Mira, on which we briefly comment, one can describe the sources in terms of simpler objects that can be studied separately. Moreover, while lumpiness is frequently observed in AGB CSEs, it is less of a problem than in the case of Planetary Nebulae and axisymmetry usually remains a good approximation (we address this issue in Section 3).

Much of the existing literature on optical deprojection devotes particular attention to producing user-friendly algorithms with emphasis on computer time and interactivity. We do not have such ambition. Our motivation is simply to address issues of data analysis in general, and deprojection in particular, in the context of radio astronomy of evolved stars, where much of the current literature is limited to displaying channel and spectral maps. We also mean to show that much information can be obtained by constructing simple variables and simple histograms that do not require complex analysis tools. More generally, the paper is written in the spirit of encouraging more quantitative analyses than commonly found in analyses of radio observations of evolved stars using instruments that do not have as good sensitivity and resolution as ALMA is now offering.

The paper is organized as follows: in Section 2, we explore the more important features of the problem of deprojection using simulated observations; in Section 3, we apply the information obtained in the first part to a few actual stars; Section 4 summarizes the two preceding sections and makes some statements aimed at helping and guiding future analyses of millimetre/sub-millimetre observations of the CSEs of axisymmetric radio sources.

For an easier reading, we have collected in an appendix many developments, which, although important for an in-depth understanding, are not essential for grasping the main message.

2 AN EXPLORATION OF THE MAIN FEATURES USING SIMULATED OBSERVATIONS

2.1 Transformation relations between space and star coordinates

We define (Figure 1) two orthonormal coordinate systems, (x, y, z) and (ξ, η, ζ) ; (x, y, z) with x along the line of sight (positive away from the observer), y pointing east and z pointing north; (ξ, η, ζ) with ξ along the star axis obtained from (x, y, z) by a first rotation of angle ψ about x and a second

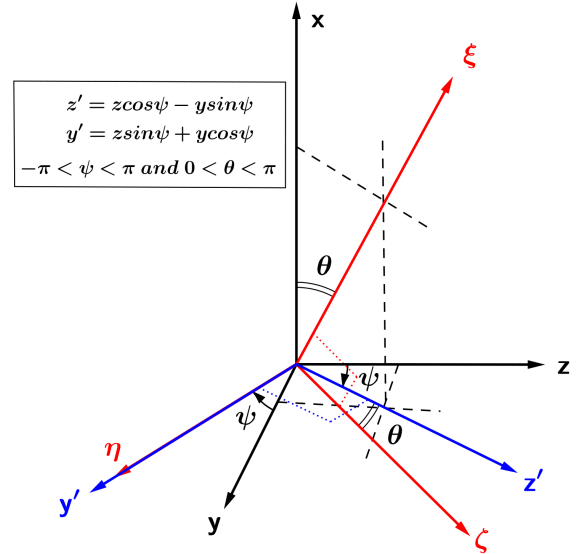


Figure 1. Coordinate transformations.

rotation of angle θ about y' , the transformed of y in the first rotation. Transformation relations between the two systems are spelled out in Appendix A1. We also use polar coordinates (R, φ) in the plane of the sky:

$$\begin{aligned} y &= R \cos \varphi \\ z &= R \sin \varphi \end{aligned} \quad (3)$$

and we define

$$r = \sqrt{x^2 + y^2 + z^2} \quad (4)$$

2.2 Effective emissivity, wind velocity and their symmetries

The flux densities, $f(y, z, V_x)$ or $f(R, \varphi, V_x)$, available to analysis are three-dimensional objects, which makes their visualization difficult. Traditionally, one uses channel-maps (z vs y distributions in each V_x bin or group of neighbour bins) or spectral maps (V_x distributions in each pixel or group of neighbour pixels). However, when the number of velocity bins and of pixels is large, it becomes increasingly difficult to obtain useful information by direct inspection of an increasingly large number of maps. It is therefore convenient to reduce the problem to two dimensions by introducing moments of order k obtained by integrating the measured flux densities over one of the variables after having multiplied them by that variable raised to power k . In practice, only a few of these moments are commonly used, usually under other names. Integrating over V_x maps the flux

$$F(R, \varphi) = \int_{-\infty}^{+\infty} f(R, \varphi, V_x) dV_x \quad (5)$$

As $\rho(x, y, z)$ decreases usually rapidly with r , typically as r^{-2} , mapping the quantity $\int R f(R, \varphi, V_x) dV_x$ is better suited for revealing finer details of the flux map. The first order moment

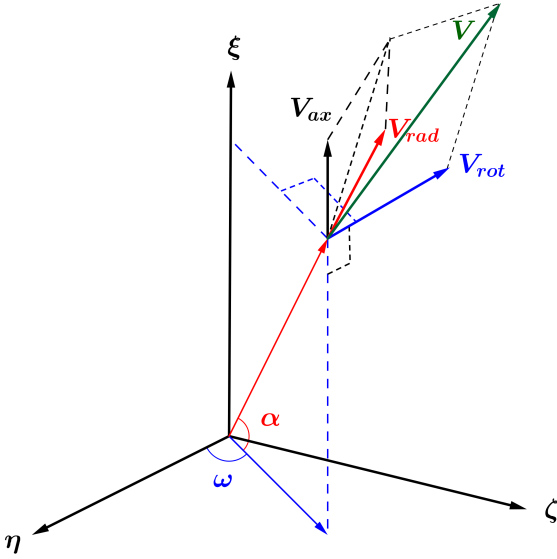


Figure 2. Wind velocity components.

divided by the integrated flux

$$\langle V_x \rangle = \frac{\int_{-\infty}^{+\infty} V_x f(y, z, V_x) dV_x}{F(y, z)} \quad (6)$$

gives the mean Doppler velocity in each pixel, which is a useful indicator of a possible asymmetry of the wind velocities. Similarly, $\langle |V_x| \rangle$ and $\langle V_x^2 \rangle$ provide useful information.

Fixing a sky coordinate, y or z , or integrating over it corresponds to the P-V diagrams commonly used in astronomy. As the dependence on φ of the flux densities is often only weakly coupled to its dependence on R (to the extent that the dependence on stellar latitude of the star properties is only weakly coupled to its dependence on r) polar coordinates are better suited to such analyses, displaying quantities such as $\int_0^{+\infty} f(R, \varphi, V_x) dR$ and $\int_0^{+\infty} R f(R, \varphi, V_x) dR$.

It is convenient to express the components of the wind velocities in the star frame (Figure 2). Their symmetry properties are detailed in Appendix A2. Precisely, we define a radial component V_{rad} , an axial component V_{ax} along the star axis and a rotation component about the star axis, V_{rot} . In terms of the stellar latitude α and stellar longitude ω , the (ξ, η, ζ) components of the wind velocity are therefore $(\xi, \eta, \zeta)V_{rad}$; $(1, 0, 0)V_{ax}$; and $(0, -\sin \omega, \cos \omega)V_{rot}$ respectively and the Doppler velocity reads:

$$V_x = \frac{x}{r} V_{rad} + \cos \theta V_{ax} - \frac{R \cos(\varphi - \psi) \sin \theta}{r \cos \alpha} V_{rot} \quad (7)$$

2.3 Velocity spectra and P-V diagrams

For stars that have lived long enough on the AGB for the morphology of their gas envelope to be significantly altered, the sky map of the measured flux, $F(y, z)$, directly reveals the projection of the star axis on the sky plane. However, this is often not the case for AGB stars having mass loss rate at the scale of $10^{-7} \text{ M}_{\odot} \text{ yr}^{-1}$ or smaller: they display

spherical morphology and axial symmetry, if present, can only be revealed from the velocity distribution of the wind.

However, mapping the mean value $\langle V_x \rangle$ of the gas velocity on the sky plane is not sufficient to find the projection of the star axis. Expansion and rotation combine with different symmetry properties, resulting in an apparent tilt of the projection of the star axis on the sky plane, by an unknown amount. It is only in the cases of pure rotation and pure expansion that the axis of the star is an axis of symmetry of the sky map. However, in such cases, this axis of symmetry is the projection of the star axis in the case of pure expansion, but is perpendicular to it in the case of pure rotation. It is therefore necessary, in order to evaluate the value of ψ , the position angle of the projection of the star axis on the sky plane, to exploit the information contained in the velocity spectra rather than integrating over velocities.

We illustrate this point with a series of simulations, the results of which are displayed in Figure 3. In this figure, the angle φ is the position angle of the pixel on the sky map. The positive y axis has $\varphi = 0$, the positive z axis has $\varphi = 90^\circ$, etc. The Doppler velocity V_x is measured positive when red shifted. Figure 3 includes six different sets, each associated with a particular orientation θ of the star axis. The position angle of the projection of the star axis on the sky plane is always $\psi = 0$, meaning pointing north. Changing its value results simply in a rotation of the sky map about the origin, meaning a simple translation of the φ vs V_x P-V diagrams along the φ axis. The inclination of the star axis with respect to the line of sight (x axis) is measured by the angle θ indicated on the figure, between 15° and 90° in steps of 15° . For $\theta = 0$ the star is seen pole on; for $\theta = 90^\circ$ the observer is in the equatorial plane of the star.

Simulations are made for three cases, each corresponding to a column: pure expansion on the left, a combination of expansion and rotation in the middle and pure rotation on the right. The star properties are supposed to be invariant under rotation about the star axis. The effective emissivity is taken isotropic with dependence in r^{-2} on the distance r from the star. Two different forms, *A* and *B*, are used to define the dependence of the gas velocity on the star latitude, each corresponding to a row in the figure. The velocities are otherwise supposed to be independent of the star longitude (imposed by rotational invariance) and of the distance r to the star (the absence of velocity gradients is a simplification expected not to have important consequences on the qualitative comments made here). Moreover, they are supposed to be symmetric with respect to the equatorial plane, implying central symmetry when combined with rotational invariance, meaning that changing (x, y, z) in $(-x, -y, -z)$ leaves the effective emissivity invariant and changes the sign of the gas velocity. This corresponds to adding 180° to φ and its effect is immediately visible in Figure 3. The expansion velocity V_{rad} is taken purely radial and the rotation velocity V_{rot} is taken perpendicular to the star axis. In both cases *A* and *B*, rotation is enhanced near the equator and expansion is enhanced near the poles. For each value of θ the upper row is for case *A*,

$$\begin{aligned} V_{rad} &= V_0 \sin^2 \alpha \\ V_{rot} &= V_0 \cos^2 \alpha \end{aligned} \quad (8)$$

In the lower row, case *B*, V_{rad} is set to 0 and V_{rot} to V_0 for $\alpha < 45^\circ$ while V_{rot} is set to zero and V_{rad} to V_0 for $\alpha > 45^\circ$

(Figure 4). Each simulation is illustrated by two panels. The upper panel is the P-V diagram, ϕ vs V_x , with the abscissa running from -10 km s^{-1} to 10 km s^{-1} and the ordinate from 0 to 360° ; the lower panel is the projection of the diagram on the velocity axis.

In order to construct an axially symmetric model of the CSE of the star, one needs to find the position of the star axis in space, namely the values of θ and ψ , before evaluating the values of the effective emissivity and gas velocity as a function of the star latitude α and the distance r to the star. Once ψ is known, one can rotate the data on the sky map in order to have $\psi = 0$, namely the projection of the star axis pointing north. Then the star properties display simple symmetries with respect to transformation S_1 , changing (x, y, z) in $(-x, y, -z)$ and transformation S_2 , changing (x, y, z) in $(x, -y, z)$; the Doppler velocity is even under S_1 and odd under S_2 for pure rotation and even under S_2 and odd under S_1 for pure expansion. These symmetries are clearly seen in Figure 3 in the cases of pure expansion (left columns) or pure rotation (right columns). However, if one does not know the value of ψ (and one has no reason to know it a priori), the symmetry obeyed by the Doppler velocity as a function of ϕ does not tell the value of ψ : the values associated with pure expansion and pure rotation differ by 90° . It is then essential to make a distinction between the effects of expansion and rotation on the Doppler velocity and the P-V diagrams before having a chance to measure ψ . Assuming that we know θ and ψ , and given the dependence on r and α of the effective emissivity and of the gas velocity, one can calculate, for each panel of Figure 3, the flux density $f(y, z, V_x) = \rho(x, y, z) dx/dV_x$ for each pixel (y, z) , or equivalently (R, ϕ) . Further details are given in Appendix A3.

2.3.1 The case $\theta = 0^\circ$

In this case, the flux density is independent of ϕ : the whole information is contained in the projections on the V_x axis of the P-V diagrams. Moreover, the rotation velocity being perpendicular to the line of sight does not contribute to the Doppler velocity: for pure rotation, V_x identically cancels. A consequence is that the mixed case is identical to the pure expansion case.

When attempting to construct a model, there exists no constraint imposed on the forms chosen for the radial and axial components of the velocity vector (see Sub-section 2.2), respectively $V_{rad}(r, \alpha)$ and $V_{ax}(r, \alpha)$ (not to mention V_{rot} , which can take any value!). In particular, the hypothesis of rotational invariance is of no use in this case: all it says is that the measured flux density $f(R, \phi, V_x)$ must be independent of ϕ . Either it is, in which case the data are consistent with the hypothesis, or it is not, in which case they are not.

In summary, when $\theta = 0^\circ$, there is nothing to be learned about rotation and about the dependence of the expansion velocity on the star latitude and the distance from the star. But when making assumptions, on the basis of physics arguments, about the form they take, one can reconstruct the values of the effective emissivity and expansion velocity at any point in space. If one assumes that ρ , V_{rad} and V_{ax} depend only on r the integral equation is easily solved to give $\rho(r)$ for any r value. Then, assuming particular forms for the r dependence of $V_{rad}(r)$ and $V_{ax}(r)$, one can also calculate

them for any r value. In such a case, one obtains a spherical model of the CSE.

2.3.2 The case $\theta = 90^\circ$

In this case, as $R < r$, the angle ϕ measures the maximal value taken by the stellar latitude α in a given pixel (for $x = 0$):

$$r \sin \alpha = z = R \sin \phi \quad (9)$$

In the case of pure expansion, as $V_x = (x/r)V_{rad}$, the Doppler velocity tends to V_{rad} when x is large. Near the y axis, $\phi = 0^\circ$, one is probing low latitudes where V_{rad} cancels. On the contrary, near the z axis, $\phi = 90^\circ$, one is probing large latitudes where V_{rad} takes its maximal values. The maximal values of V_x are therefore reached around $\phi = 90^\circ$ and the minimal values around $\phi = 0$. The precise value taken by V_x at maximum depends on the dependence of V_{rad} over α , the larger the more concentrated near the poles are high V_{rad} values.

In the case of pure rotation, as

$$V_x = -\frac{R \cos \phi}{r \cos \alpha} V_{rot} \quad (10)$$

the $\cos \phi$ term modulates the maximal value of V_x as a function of ϕ : it oscillates between $-R(r \cos \alpha)^{-1} V_{rot}$ and $+R(r \cos \alpha)^{-1} V_{rot}$ when ϕ goes from 0 to 180° , cancelling at $\phi = 90^\circ$. When $\theta = 90^\circ$, contrary to the previous case ($\theta = 0^\circ$), rotational invariance cannot be verified but, if it is assumed to be obeyed, it strongly constrains the data. It implies that for a given value of z , the effective emissivity is a function of only r and $\sin \alpha = z/r$, namely of r alone. Therefore, for each value of z , one can write

$$F(y, z) = \int \rho(r, z) dx = \int \rho(r, z) r (r^2 - R^2)^{-1/2} dr \quad (11)$$

an integral equation easily solvable by iteration. This property has been known for a long time and is being applied extensively in deprojection algorithms used in optical astronomy (Wenger et al. 2013, and references therein). Rotational invariance constrains the dependence of $F(y, z)$ on y for each value of z . Similarly, for each value of z , V_{rad} and V_{rot} depend only on r , so does therefore dx/dV_x . Assuming particular forms for the r -dependence of V_{rad} and V_{rot} , one can then evaluate their values at each point in space. More precisely, for each value of z , as long as the forms chosen for V_{rad} and V_{rot} depend on a small enough number of parameters compared with the number of pixels, one can calculate the values taken by these parameters and obtain V_{rad} and V_{rot} as functions of r and $z = r \sin \alpha$, namely as functions of r and α .

In summary, when $\theta = 90^\circ$, one cannot verify the validity of the hypothesis of rotational invariance (even if one can infer its absence when $F(y, z)$ and $F(-y, z)$ are not equal). But, assuming it, one can evaluate the effective emissivity at any point in space. One can also evaluate the values taken by V_{rad} and V_{rot} at any point in space once arbitrary forms, chosen according to physics arguments, have been adopted for their r -dependence, but V_{ax} can take any arbitrary value.

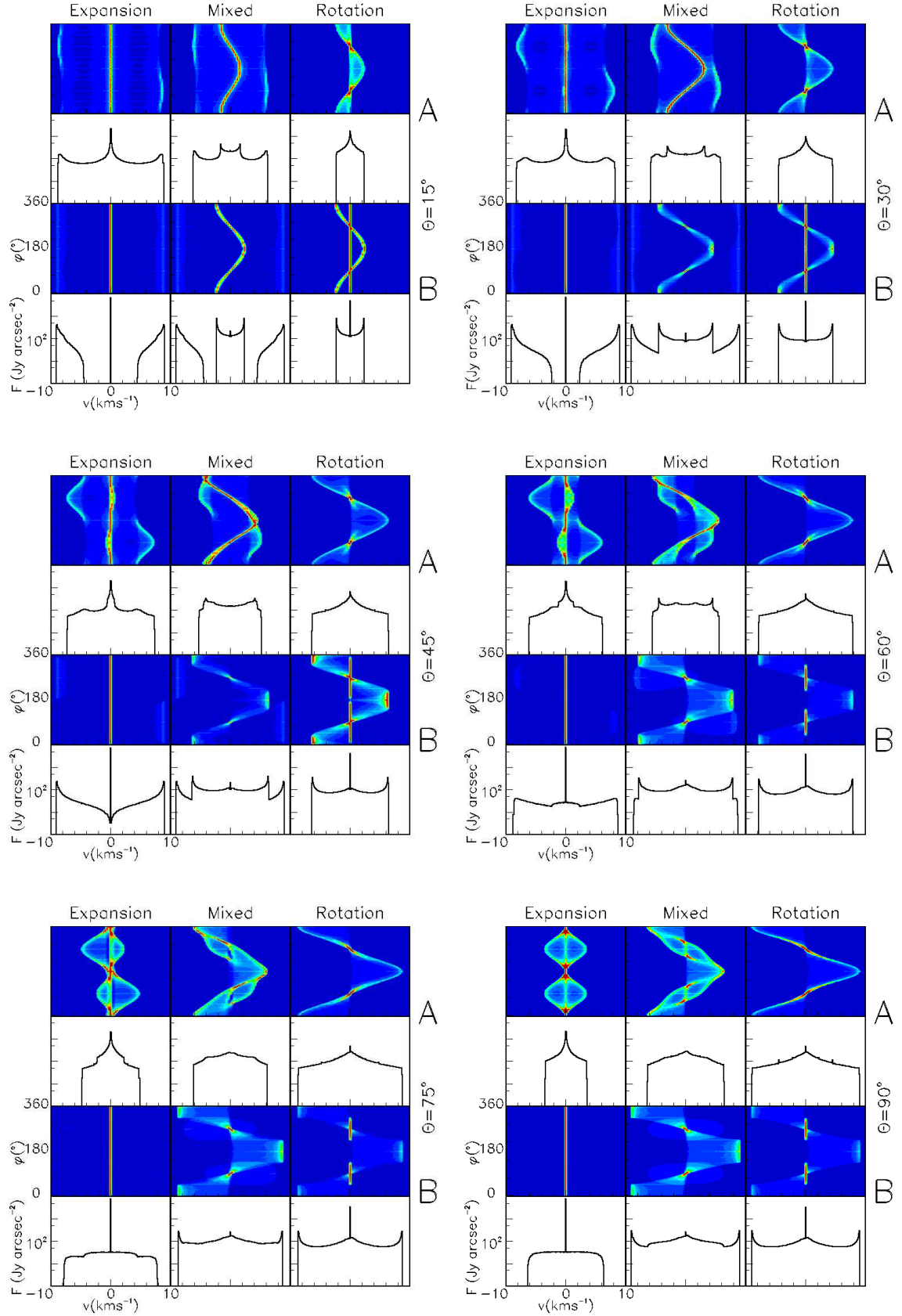


Figure 3. P-V diagrams. The spikes observed at $V_x = 0$ in the pure expansion and pure rotation cases correspond to the contributions of respectively $V_{rot} = 0$ and $V_{rad} = 0$: in such cases, the outside and respectively inside volumes of the cone do not emit, this absence of emission causes the spikes. In the mixed case, both the inside and outside volumes emit.

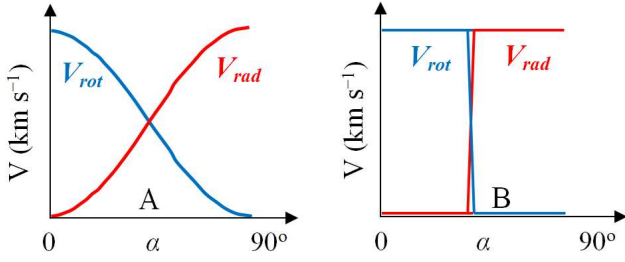


Figure 4. Dependence of gas velocity (rotation in blue, expansion in red) on star latitude in cases *A* and *B* used in the simulation.

2.3.3 Pure rotation and pure expansion

In a given pixel, both pure rotation and pure expansion typically generate double-horned spectral distributions. Indeed, if V_{\max} is the maximal value taken by $|V_x|$ in this pixel, $dN/dV_x = (dN/dx)(dx/dV_x)$ is infinite at $V_x = V_{\max}$ where $dV_x/dx = 0$. A simple illustration is obtained using $V_{\text{rot}} = V_0 \cos \alpha$ and $V_{\text{rad}} = V_0$. The corresponding spectral distributions are respectively proportional to $(V_{\max}^2 - V_x^2)^{-1/2}$ and $(V_{\max}^2 - V_x^2)^{-3/2}$. The limits of the spectrum are $\pm V_{\max}$, with $V_{\max} = V_0 \cos \phi \sin \theta$ for pure rotation and $V_{\max} = V_0$ for pure expansion. In both cases, the spectrum grows from its value at $V_x = 0$ to infinity at the limits. Details are given in Appendix A4.

2.3.4 Mixing rotation and expansion

The simplest case is case *B*: x probes either inside the cone where it sees only expansion or outside where it sees only rotation. Hence, for case *B*, the middle columns of Figure 3 are simply the superposition of the left and right columns. This remains qualitatively true when the regions probed by x are dominated by a single regime, rotation or expansion, respectively near the equator or near the poles. However, in general, for a given pixel, V_x receives significant contributions from both rotation and expansion. As a result, when mapping $\langle V_x \rangle$, one sees a symmetry that reflects both the value of ψ and the relative importance of rotation and expansion: Figure 5 illustrates the difficulty of finding the axis of the star when nothing is known a priori about their relative contributions. The next sections (2.3.5, 2.4 and 2.5) address issues related to this problem, the nature of which deserves some preliminary comments.

A first remark is that we are concerned here with the kinematics of the CSE, not its morphology, motivated by the fact that many low mass-loss rate AGB stars display an essentially spherical morphology. If such is not the case, namely if axisymmetry is already revealed by the morphology, so much the better: the projection of the star axis on the sky plane will be immediately identified. But the general problems of measuring the inclination θ of the star axis with respect to the line of sight and of telling expansion from rotation will remain. For this reason, we assume in what follows that the effective emissivity is spherically symmetric.

A second remark is related with understanding what is causing the apparent tilt of the star axis in Figure 5. For such a tilt to take place, as already mentioned, two conditions must be obeyed: both rotation and expansion must

be present and θ must differ from both 0° and 90° . But a third condition is also mandatory: expansion must deviate from isotropic, namely be bipolar (isotropic expansion contributes equally to positive and negative values of V_x , causing the mean to cancel). All three conditions make sense from a physics point of view and detecting the possible simultaneous presence of rotation and expansion is a difficult but important task in AGB astrophysics. Taking the z axis as star axis, the velocity fields of expansion and rotation have different symmetries: rotation is symmetric about the y axis and antisymmetric about the z axis, expansion is symmetric about the z axis and antisymmetric about the y axis. Namely, in the case of pure rotation, the projection of the star axis on the sky plane is perpendicular to the symmetry axis of the map, while in the case of pure expansion it is the symmetry axis of the map. In general, in a given pixel, $\langle V_x \rangle$ receives contributions from both expansion and rotation, respectively $V_1 = \langle x V_{\text{rad}}/r \rangle$ and $V_2 = R \cos \phi \sin \theta \langle V_{\text{rot}}/r \cos \alpha \rangle$. Assuming that both V_{rad} and V_{rot} are independent of r and even functions of $\sin \alpha$, the problem is scale invariant and V_1 , V_2 and their sum do not depend on R , but only on ϕ . This is immediately apparent on Figure 5. While V_1 is symmetric about $\phi = 90^\circ$, V_2 is symmetric about 0° . But their sum, in general, has no reason to display any symmetry. Indeed the apparent symmetry of the map displayed in Figure 5 is only approximate and the symmetry is in fact destroyed rather than the symmetry axis being simply tilted.

A third remark is that while pure rotation splits the sky map in two regions, one blue-shifted on one side of the projection of the star axis on the sky plane, the other red-shifted on the other side, pure expansion can generate both blue-shifted and red-shifted velocities in a same pixel if the polar outflows are broad enough. This is clearly seen in Figure 3, particularly for large values of θ .

2.3.5 Evaluating the value of the position angle ψ of the projection of the symmetry axis on the sky plane

When $\psi = 0$, in the vicinity of the y axis, changing z in $-z$ leaves the velocity spectrum unchanged in the case of pure rotation but reflects it about the origin in the case of pure expansion. Similarly, in the vicinity of the z axis, changing y in $-y$ leaves the velocity spectrum unchanged in the case of pure expansion but reflects it about the origin in the case of pure rotation. Appendix A5 introduces a function χ_ψ^2 of the position angle constructed on this remark, which is meant to reach its minimum at ψ . However, in case *A*, when θ is sufficiently different from 0 and 90° , and when both expansion and rotation contribute significantly to V_x , χ_ψ^2 is found to be less dependent on ψ and the identification of the minimum is difficult. It is interesting to remark that a clear minimum is always found in case *B*. In this case, one is probing either the interior of the cone and sees only expansion, or the exterior of the cone, and sees only rotation: rotation and expansion never compete at a same point in space.

In practice, when there are reasons to suspect the co-existence of significant rotation and expansion velocity components, the best will be to use a model making optimal use of the known physical properties of the system and including ψ among the parameters to be adjusted by chi square minimization. An example is given in Section 3.1.

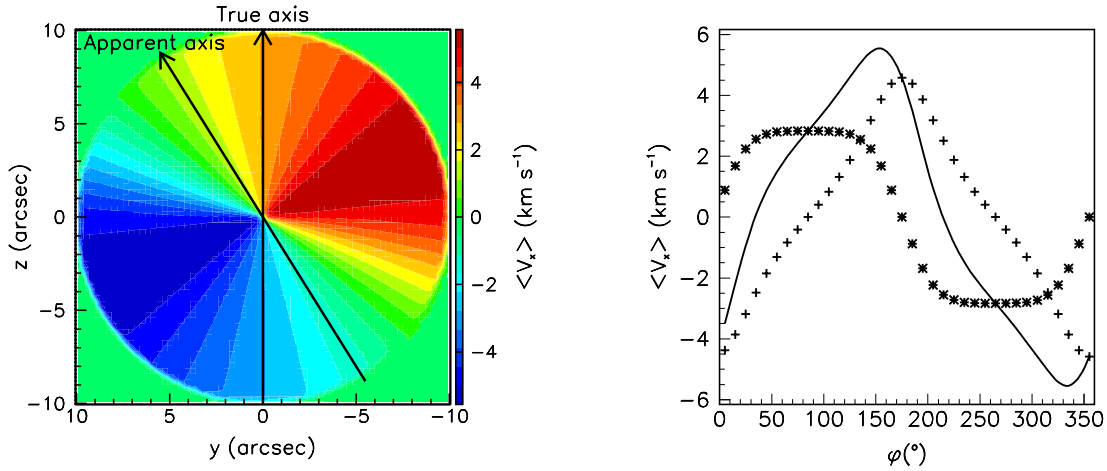


Figure 5. Mean value of the Doppler velocity, $\langle V_x \rangle$ in case A for $\theta = 45^\circ$, $\psi = 0$ and mixed expansion and rotation (middle column of the set of P-V diagrams in Figure 3). Left: its sky map; Right: its dependence on ϕ (full line) and that of the rotation (+) and expansion (*) components.

2.4 Telling rotation from expansion

Having found the value of ψ is not sufficient to tell expansion from rotation. Even in a pure case, rotation around the y axis and expansion along the z axis will both produce P-V diagrams odd under S_1 and even under S_2 . A discriminator between rotation and expansion would therefore be a useful tool. After rotation of the data on the sky plane making ψ to cancel, in the case of pure radial expansion $xV_x = (x^2/r)V_{rad}$ is positive and in the case of pure rotation $yV_x = -y^2 \sin \theta (r \cos \alpha)^{-1} V_{rot}$ has the sign of $-V_{rot}$. Appendix A6 makes use of this property to construct a function of ϕ , $A(\phi)$, as a possible discriminator between rotation and expansion. The values of $A(\phi)$ at $\phi = 0^\circ$ and $\phi = 90^\circ$ or its integral over ϕ are generally good indicators of the relative importance of rotation over expansion. However, when dealing with a small perturbation to a global isotropic expansion, it is difficult to assert its precise nature, rotation or bipolar expansion. Here again, as in the preceding sub-section, the use of a model adjusted to best fit the data will often be the most efficient method. It will include what is known of the physical properties of the system, in particular the likely form taken by the radial dependence of the rotation and expansion velocities. The radial dependences of the rotation velocity (typically Keplerian or decreasing faster at large distances) and of the expansion velocity are indeed important quantities to evaluate. We address briefly the issue in Section 3, in the context of RS Cnc and L1527 but a general treatment is beyond the scope of the present article. Our choice in the present section (constant rotation and expansion velocities) is motivated by simplicity and by the fact that it has little impact on the general qualitative ideas developed in the article because of the rapid radial decrease of the effective emissivity. In practice, preconceived ideas about the radial dependences of the rotation and expansion velocities, based on physics arguments, will help with the solution of the problem.

2.5 Inclination θ of the star axis with respect to the line of sight

Having evaluated the value of ψ and assuming for simplicity that $\psi = 0$, one needs to evaluate the value of the inclination θ of the star axis with respect to the line of sight. For the star axis to be well defined, there must be a large enough asymmetry of the effective emissivity and/or the wind velocity: spherical distributions prevent the definition of such an axis. As a result, what can be generally measured is the product of a measure of the inclination, typically $\sin \theta$, by a measure of the elongation of the effective emissivity and/or velocities along the star axis. This result, which is well known for morphology (Steffen et al. 2011; Leahy 1991; Palmer 1994; Magnor et al. 2004 & 2005) is also valid for kinematics. As detailed in Appendix A7, this implies strong correlations relating the inclination angle to the elongation of the outflow on the star axis, namely the ratio of polar to equatorial wind velocities.

2.6 Radial dependence of the CSE properties

One expects the R -dependence of the integrated flux to carry much information about the r -dependence of the effective emissivity. Indeed, from pure dimensional considerations, one would expect a r^{-n} dependence of the effective emissivity to produce a $R^{-(n-1)}$ dependence of its integral on the sky map. As detailed in Appendix A8, this is generally the case. Similarly, the sky map of the mean of the absolute value of the Doppler velocity is found to reveal directly the presence of velocity gradients.

These results illustrate further the advantage of displaying the measured flux densities in terms of polar rather than Cartesian coordinates on the sky plane. Their dependence on R is related simply to the dependence on r of the effective emissivity and wind velocity, while their dependence on ϕ is related to the dependence of the effective emissivity and wind velocity on the orientation of the star axis and on star

latitude. Without having recourse to a model, much information about the morphology and kinematics of the CSE can be obtained from simple quantities constructed directly from the expression of the flux densities in polar coordinates.

3 APPLICATION TO REAL OBSERVATIONS

3.1 A typical AGB star: RS Cnc

As a first application of the results of the preceding sections, we consider a typical AGB star, RS Cnc that has been studied in some detail, in particular from observations of CO(1-0) emission using the Plateau de Bure Interferometer (Hoai et al. 2014; Nhung et al. 2015a).

Figure 6 displays the dependence on R and ϕ of the measured flux multiplied by R . The R -dependence is well described by a power law of the form $R^{-0.63}$ implying a r -dependence of the effective emissivity of the approximate form $r^{-1.6}$. The ϕ -dependence is very uniform, with excursions from the mean not exceeding $\sim 6\%$; Figure 6 displays also the dependence on R and ϕ of the mean Doppler velocity, which reveals a very clear north-south asymmetry.

The R -dependence suggests the presence of a significant negative velocity gradient, at variance with the results of the best fits published earlier (Nhung et al. 2015a), which imply a positive velocity gradient both at the equator and near the poles. This is a good illustration of a general situation and deserves therefore a detailed analysis. The model of Nhung et al. (2015a) assumes a stationary regime: a radial wind velocity decreasing with r implies a product dr^2 (d is the gas density) increasing with r at the same rate. However, the dependence on r of the effective emissivity includes in addition a temperature factor (that accounts for the population of the emitting quantum state and the probability of emission) and a UV dissociation factor. In the model of Nhung et al. (2015a), the radial dependence of the temperature is discussed in detail, using in particular the ratio of CO(2-1) and CO(1-0) emission, and the UV dissociation factor is taken from the literature. Both decrease strongly with r . As a result, the product ρr^2 (ρ is the effective emissivity) decreases with r because the contributions of the temperature and of UV dissociation win over the contribution of stationarity. The hypothesis of stationarity links the radial dependence of ρr^2 to that of $\langle |V_x| \rangle$, which receives therefore three contributions: a 1.9%/arcsecond decrease from temperature, a 3.4%/arcsec decrease from UV dissociation and 1.8%/arcsec increase from the velocity gradient, adjusted to best fit the observed 3.5%/arcsec negative velocity gradient observed in the data. The result of Nhung et al. (2015a) is therefore perfectly consistent with the observation of a negative velocity gradient made here, the reason being that the two velocity gradients measure in fact different quantities, the result of Nhung et al. (2015a) resting heavily on the hypothesis of a stationary flow.

The question then arises of the validity of the assumption of stationarity used in the model: the radial scale spanned by Figure 6 means some 10^5 years, the wind velocity might have increased somewhat over such a long period, implying higher gas densities at large distances from the star and violating the stationarity hypothesis. To answer the question we compare the quality of two fits: one assuming stationarity and allowing for gradients on the velocities,

the other assuming instead r -independent velocities but allowing for gradients on the fluxes of matter. The best fit is obtained for the scenario that assumes stationarity, but the other fit gives a value of χ^2 that is only 12% larger. This result illustrates the difficulty to ascertain the validity of the stationarity hypothesis with confidence from the presently available observations: a dependence on age of the mass-loss rate reproduces the data nearly as well without requiring the presence of a positive velocity gradient.

RS Cnc is also a good test case to illustrate the problems associated with the measurement of the orientation of the star axis and the relative importance of expansion and rotation.

The P-V diagram displayed in Figure 7, ϕ vs V_x , shows arcs near $V_x = 0$ and at $|V_x| > 4 \text{ km s}^{-1}$ in phase opposition at a same value of ϕ , namely populating both positive and negative Doppler velocity intervals, showing, at least qualitatively, that one is dealing with expansion rather than with rotation. Moreover, the absence of significant features in quadrature, i.e. shifted in phase by $\pm 90^\circ$ with respect to these arcs, indicate that a possible contribution of rotation, if present, must be quite small (again qualitatively). The asymmetry parameter $A(\phi)$, defined in A6, reaches minimal values at the 10% level around $\phi = 0^\circ$ and $\phi = 180^\circ$ where the contribution of pure expansion cancels. To better quantify a possible contribution of rotation, we use the model described in Hoai et al. (2014) and Nhung et al. (2015a). We allow for a rotation velocity having a Gaussian dependence on $\sin \alpha$, the sine of stellar latitude, and decreasing with distance as a power of r . Calling V_{rot} the equatorial rotation velocity at $r = 1''$, σ_{rot} the σ of the Gaussian and n_{rot} the power index, we obtain a best fit for $V_{rot} = 0.4 \text{ km s}^{-1}$, $\sigma_{rot} = 0.3''$ and $n_{rot} = -1.0$. The only other parameters allowed to vary in the fit are the values of the radial expansion velocities. Figure 7 displays the dependences on ψ and θ of the best fit χ^2 , both angles being measured with an uncertainty of $\sim \pm 25^\circ$ and the values of the parameters describing the elongation along the star axis are strongly correlated with θ . Then, fixing σ_{rot} and n_{rot} at their best fit values, we obtain the dependence of the best fit χ^2 on V_{rot} displayed in Figure 7, suggesting that a rotation velocity of up to $\sim 1 \text{ km s}^{-1}$ at $r = 1''$ could be accommodated by the data. Observations, of better sensitivity than presently available would be necessary to conclude reliably on the possible presence of rotation.

3.2 The $\theta = 0$ case: EP Aquarii

EP Aqr is a textbook case of an AGB star having its axis nearly parallel to the line of sight. Its CO(1-0) and CO(2-1) emissions have been previously analysed both in terms of spherical winds and of bipolar outflows (Winters et al. 2007; Nhung et al. 2015b). We refer the reader to the respective analyses and, as in the case of RS Cnc, we limit the present discussion to issues that are of direct relevance to the considerations developed in the previous sections, in particular aiming at a unified picture of the former very different analyses. Figure 8 shows the CO(2-1) P-V diagram in the ϕ vs V_x plane and its projection on the Doppler velocity axis. As expected, it is typical of a star having its axis parallel to the line of sight. The dependence on both R and ϕ of the measured flux multiplied by R is dominated by important inhomogeneities that extend up to large

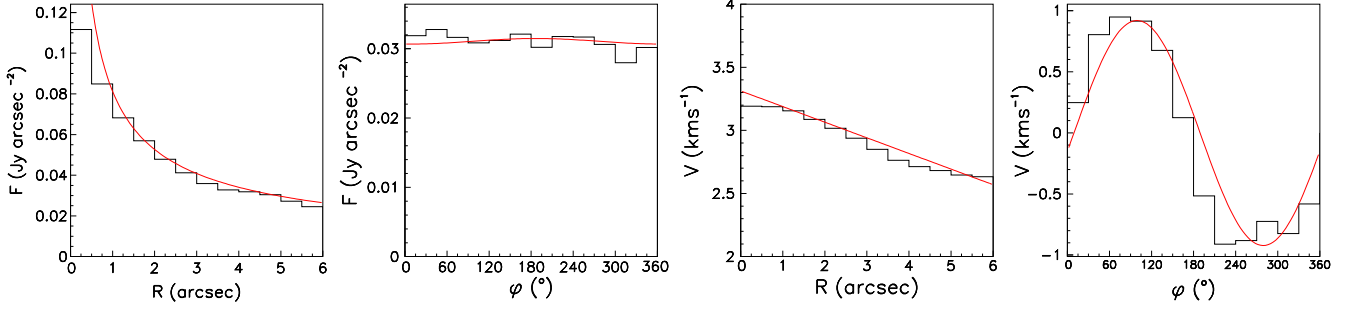


Figure 6. Measured CO(1-0) flux of RS Cnc. Left: R -dependence of $F(y,z)$ averaged over ϕ ; the fit (in red) is a power law of index -0.63 . Central left: ϕ -dependence of $F(y,z)$ averaged over R ; the fit (in red) is a sine wave of amplitude 1.3% of the mean value. Centre right: R -dependence of $\langle V_x \rangle$ averaged over ϕ ; the fit (in red, excluding the first bin) is linear, with a slope of -0.12 km s^{-1} per arcsecond. Right: ϕ -dependence of $\langle V_x \rangle$ averaged over R ; the fit (in red) is a sine wave of amplitude 0.92 km s^{-1} and phase of 6° .

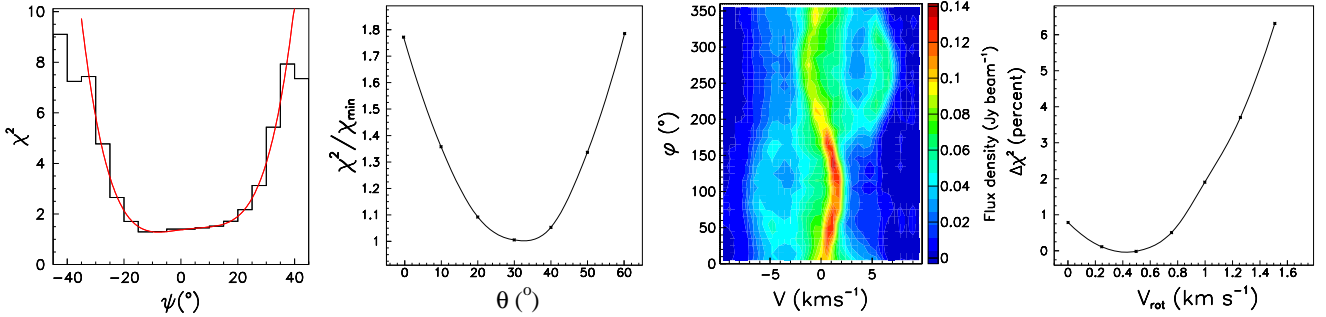


Figure 7. RS Cnc. From left to right: dependences on ψ and on θ of the best fit χ^2 normalized to its minimal value; P-V diagram, ϕ vs V_x ; dependence of the best fit χ^2 (in percent excess with respect to its minimal value) on the rotation velocity.

radii. The R -dependence is steeper for CO(2-1) than for CO(1-0) as expected, with respective power indices -1.2 and -0.9 . The sky maps of the mean Doppler velocity display a small north-west/south-east asymmetry, interpreted by Nhung et al. (2015b) as resulting from the small inclination of the star axis on the line of sight.

In the $\theta = 0$ approximation the stellar longitude ω is equal to the sky position angle ϕ of the pixel and the stellar latitude α is related to x by the relation $x = R \tan \alpha$. The relation $f(R, \phi, V_x) dV_x = \rho(r, \alpha, \omega) dx$ can then be dealt with in each $\phi = \omega$ interval separately. As rotation cannot be detected, we assume a radial wind of velocity V_{rad} . Using the relations

$$\begin{aligned} V_x &= V_{rad} \sin \alpha \\ x &= r \sin \alpha \\ R &= r \cos \alpha \end{aligned} \quad (12)$$

one can associate in each pixel a value of x to each value of V_x if we know V_{rad} : x is solution of the equation

$$rV_x = \sqrt{x^2 + R^2} V_x = xV_{rad} \quad (13)$$

namely

$$x = \frac{V_x}{\sqrt{V_{rad}^2 - V_x^2}} R \quad (14)$$

knowing x one also knows $r = \sqrt{x^2 + R^2}$ and $\sin \alpha = x/r$.

An estimate of the effective emissivity averaged over

stellar latitude (corresponding to spherical symmetry of the effective emissivity), $\rho^*(r)$, can be obtained from the flux measured in each pixel, $F(y,z) = \int \rho(r, \alpha, \omega) dx$. In each $\phi = \omega$ interval, one obtains $\rho^*(r)$ by solving the integral equation

$$F(R) = \int \rho^*(r) dx = 2 \int \rho^*(r) r (r^2 - R^2)^{-1/2} dr \quad (15)$$

where the second integral runs from R to $13''$, the mean distance at which CO molecules are UV-dissociated. Assuming in each ϕ bin a form (r measured in arcseconds).

$$\rho^*(r) = \rho_0^* r^{-n^*} \quad (16)$$

good fits are obtained and the dependence on ϕ of ρ_0^* and n^* is displayed in the right panels of Figure 8. The r -dependence of the effective emissivity is steeper for CO(2-1) than for CO(1-0) and its slope reaches a maximum in the north direction for both lines. The relation $f(R, \phi, V_x) \Delta V_x = \rho(r, \alpha, \omega) \Delta x$ where Δx is the x interval spanned by a velocity bin ΔV_x can then be used in each (R, ϕ) bin to evaluate the radial expansion velocity, V_{rad} , as a function of x in the approximation where the effective emissivity is taken in each ϕ bin equal to $\rho_0^* r^{-n^*}$ as evaluated in the previous paragraph. For the purpose of illustration, we do so over the whole ϕ range but it can as well be done in each ϕ bin separately when the data are of sufficient quality. In order to exclude the equatorial region, where the evaluation of V_{rad} is less reliable, we limit the stellar latitude to the range $|\sin \alpha| > 0.3$ ($|\alpha| > 17.5^\circ$), with the effect of excluding low values of r (typically smaller than $0.8''$). Figure 9 shows the resulting distribution of V_{rad} ,

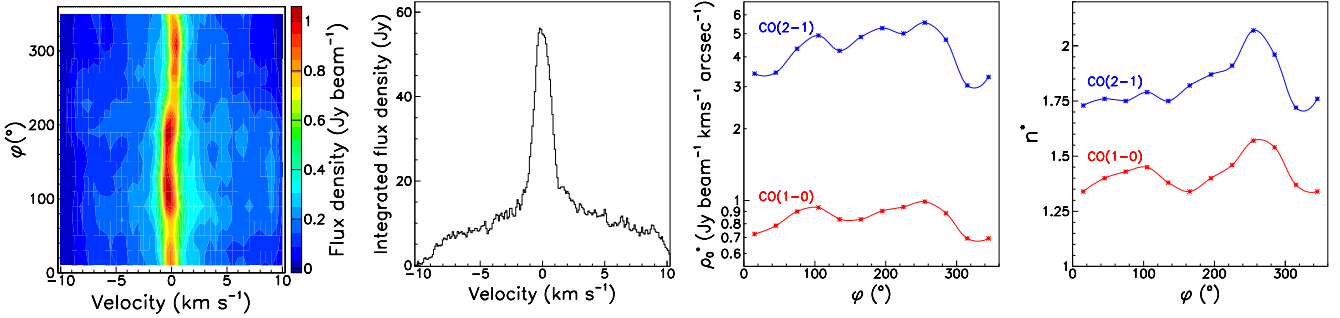


Figure 8. EP Aqr, from left to right: P-V diagrams in the ϕ vs V_x plane of the CO(2-1) data; its projection of the V_x axis; dependence on ϕ of ρ_0^* (centre right) and n^* (right) for CO(1-0) (red) and CO(2-1) (blue) observations.

averaged over ϕ , in the stellar meridian plane. It gives evidence for a strong polar enhancement, at variance with a weak radial dependence up to $r \sim 8''$. It provides a unified picture of the two models that have been proposed earlier, the model of Winters et al. (2007) corresponding to V_{rad} dependent on r but independent on α , that of Nhung et al. (2015b) corresponding to V_{rad} dependent on α but independent on r . The projections of the V_{rad} distributions on the $\sin \alpha$ and r axes illustrate the preference for the latter over the former.

3.3 The radial expansion representation

The analysis presented in the preceding section can be applied to any observation: it is always possible to calculate, given a value of V_{rad} , for each pixel and each Doppler velocity, the quantity

$$x = rV_x/V_{rad} = \frac{V_x}{\sqrt{V_{rad}^2 - V_x^2}} R \quad (17)$$

and obtain this way a 3-D representation of the observation, with each point (x, y, z) given an effective emissivity

$$\rho(x, y, z) = f(y, z, V_x) dV_x/dx = \frac{x(V_{rad}^2 - V_x^2)}{r^2 V_x} f(y, z, V_x) \quad (18)$$

Such a representation will have something to do with reality if the kinematics is indeed dominated by a radial expansion with constant velocity V_{rad} . In practical cases, this may often be approximately the case, at least locally in some domain of the (y, z, V_x) space. In such cases, it is usually possible to have an estimate of the range in which V_{rad} may reasonably fall (clearly, V_{rad} must exceed $|V_x|$). It is then useful to have some idea of the distortion implied by the adopted representation. In particular when V_x approaches $\pm V_{rad}$. In such a case, x goes to infinity and $\rho(x, y, z)r^2$, and a fortiori $\rho(x, y, z)$, cancel. The representation becomes meaningless in this case: obviously, if there is no expansion to start with, there is no chance to learn about the morphology. However, when V_{rad} exceeds $|V_x|$ significantly, the representation is well behaved and the topology is conserved: a detached shell remains a detached shell, an isolated clump remains an isolated clump, a cavity remains a cavity. While such a representation must be interpreted with care, remembering that it is ill-behaved when $|V_x|$ approaches V_{rad} , and keeping in mind the possible presence of important distortions,

it provides a convenient 3-D visualization of the morphology, particularly useful in complex cases. Such an example is illustrated in Figure 10, displaying maps of the effective emissivity of Mira Ceti in (ξ, z) planes, with $\xi = \sqrt{x^2 + y^2}$, for various values of the angle ω between the plane and the y axis. It shows clearly the presence of arcs of detached shells.

3.4 The $\theta = 90^\circ$ case: the Red Rectangle

The Red Rectangle is a post-AGB star that has been extensively studied at optical, infrared and far infrared wavelengths. Its CO emission has been recently analysed along the lines presented in the present paper using ALMA data (Tuan-Anh et al. 2015). It has its axis nearly parallel to the sky plane and displays density and velocity configurations similar to case B considered in the preceding sections: two distinct regions with a rather sharp separation between them, a conical bipolar outflow and a rotating equatorial volume. We refer the reader to Tuan-Anh et al. (2015) for details and limit our comments to a brief summary of the main results. In the $\theta = 90^\circ$ approximation, the stellar latitude α is related to z by the relation $z = r \sin \alpha$ and the stellar longitude ω is related to y by the relation $y = r \cos \alpha \cos \omega$. Rather than dealing with independent $\phi = \omega$ intervals as in the preceding section, we deal instead with independent z intervals. Namely, in each pixel, once we know x we know

$$\begin{aligned} \sin \alpha &= z/\sqrt{x^2 + R^2} \\ \tan \omega &= x/y \end{aligned} \quad (19)$$

The measured flux is $F(y, z) = \int \rho(x, y, z) dx$: the effective emissivity expressed as a function of r and $\sin \alpha$ can be obtained from this integral equation if we assume that it is invariant under rotation about the star axis. Then, one can write

$$F(y, z) = \int \rho(r, \sin \alpha) dx = 2 \int \rho(r, z/r) r (r^2 - R^2)^{-1/2} dr \quad (20)$$

and solve the integral equation. Deprojections of optical images have been presented earlier using this same feature (see for example Wenger et al. 2013, and references therein). As two different CO lines have been observed, CO(6-5) and CO(3-2), it is possible to disentangle the effects of temperature and density and evaluate them in space as shown in Figure 11. Using the result of such deprojection, and the structure that it suggests, as guidance to define flux lines, it is then possible to construct a simple model of the wind

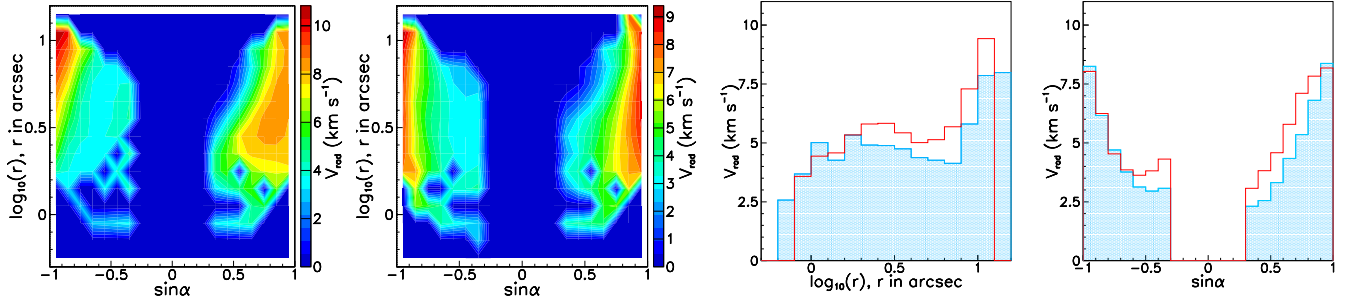


Figure 9. EP Aqr. Distribution of the radial expansion velocity V_{rad} , averaged over φ . Left: in the $(\log_{10}(r), \sin \alpha)$ plane for CO(1-0) and CO(2-1). Right: as a function of $\sin \alpha$ (centre right) and $\log_{10}(r)$ (extreme right) for CO(1-0) (red histogram) and CO(2-1) (filled blue).

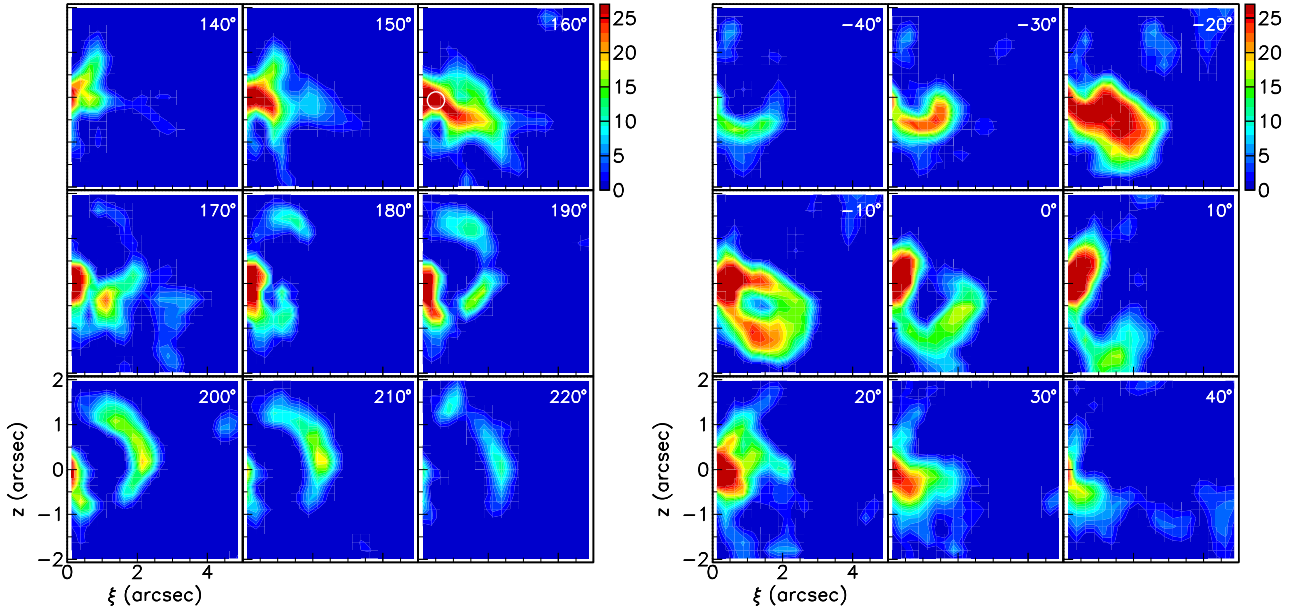


Figure 10. Western (left) and eastern (right) outflows of the central part of the CSE of Mira Ceti: maps of the effective emissivity reconstructed in space under the assumption of a pure radial expansion at constant velocity of 7 km s^{-1} . The ordinate is z and the abscissa is $\xi = \sqrt{x^2 + y^2}$. Each panel is for a 10° wide interval of ω measured clockwise from the y axis. The label in each panel gives the value of ω at the centre of the interval. The colour scale is in units of $\text{Jy km s}^{-1} \text{ arcsec}^{-3}$.

kinematics inspired from the observed morphology. It gives evidence for two well distinct volumes that host very different kinematical regimes and describes simply the radial dependence of both the expansion and rotation velocities.

3.5 Protostar L1527 IRS

Many considerations developed in the present article may in fact have applications in a much broader context. We illustrate this point in the present sub-section with the example of a young protostar, L1527 IRS. It is in its earliest stages of star formation, with a CSE of about one solar mass, and has been recently observed by Tobin et al. (2012) in the continuum (1.3 and 3.4 mm wavelength) and on the $^{13}\text{CO}(2-1)$ line at the Submillimeter Array (SMA) and the Combined Array for Research in Millimeter Astronomy (CARMA). Observations of the $\text{C}^{18}\text{O}(2-1)$ line made at ALMA have been re-

ported by Ohashi et al. (2014). All above observations have established the presence of in-falling gas onto a rotating disk surrounding the protostar and having its axis close to the y axis. Here, we use ALMA observations (2012.1.00647.S) of the $\text{C}^{18}\text{O}(2-1)$ line having a slightly better spatial resolution than those used by Ohashi et al. (2014). We refer the reader to a detailed analysis by Tuan-Anh et al. (2016). As the axis of the rotating disk is very close to the y axis, we redefine $f(y, z, V_x)$ as east-west symmetrized flux densities, $\frac{1}{2}[f(y, z, V_x) + f(-y, z, V_x)]$. Figure 12 displays maps of the integrated flux F , redefined this way, and of the mean Doppler velocity $\langle V_x \rangle$. They are dominated by rotation, red-shifted north and blue-shifted south. In the case of pure rotation about the y axis, we expect $f(y, z, V_x) = f(y, -z, -V_x)$ to cancel for $zV_x < 0$ (one side of the y axis to be blue-shifted and

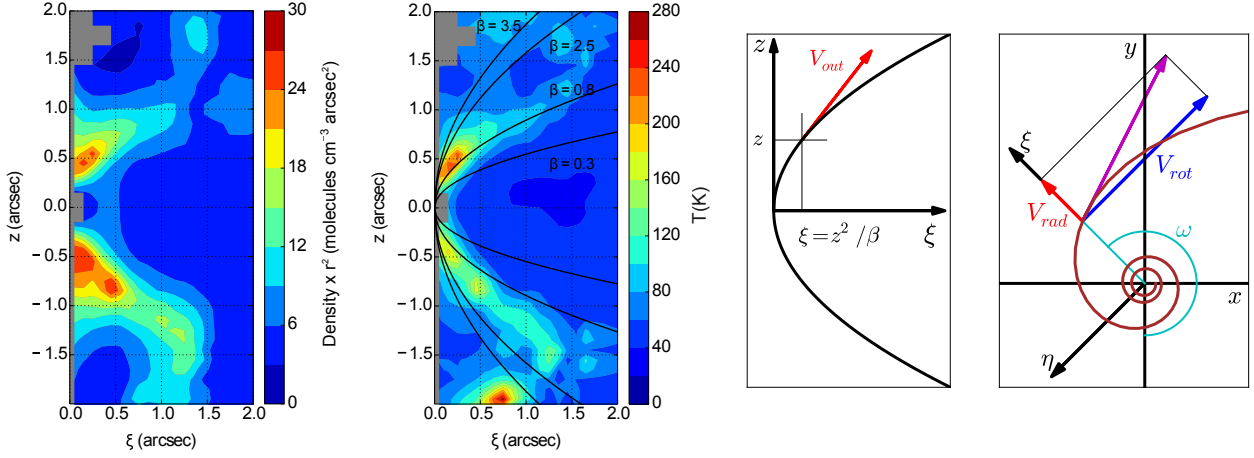


Figure 11. Red Rectangle. Left panels: maps in the half-meridian plane of the star of temperatures (extreme left) and CO density (centre left, in molecules per cm^3) multiplied by r^2 (in arcsecond 2). Right panels: wind velocity projected on the meridian plane (centre right) and the equatorial plane (extreme right). In the polar region the gas velocity V_{out} is confined to meridian planes and tangent to parabolas of equation $z^2 = \beta \xi$. Right: In the equatorial region the gas velocity is confined to planes parallel to the equatorial plane and tangent to hyperbolic spirals with a constant radial component V_{rad} and a rotation velocity V_{rot} having a power law dependence on r .

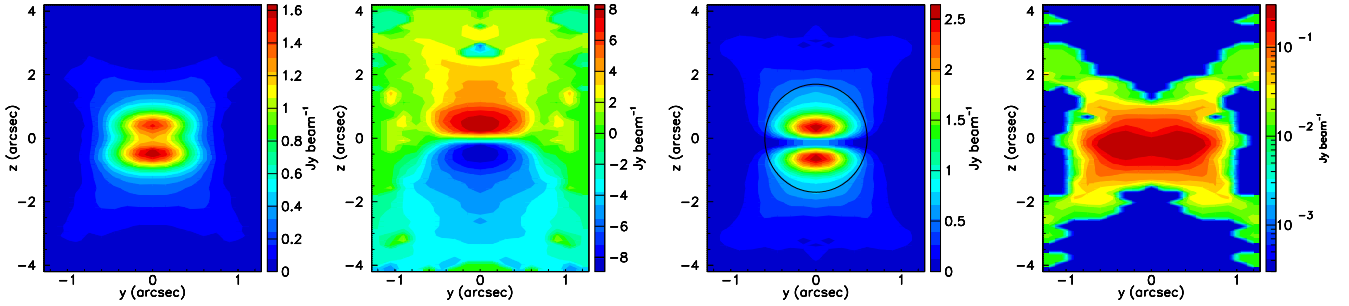


Figure 12. Protostar L1527: Sky maps of F (extreme left panel), of $\langle V_x \rangle$ (centre left panel), of F_{rot} (centre right panel) and F_{fall} (extreme right panel).

the other side red-shifted). As a result,

$$f_{rot}(y, z, V_x) = |f(y, z, V_x) - f(y, -z, V_x)| \quad (21)$$

is equal to $f(y, z, V_x)$ everywhere.

On the contrary, in the case of pure in-fall, $f_{rot}(y, z, V_x) = 0$. We may then define

$$f_{fall}(y, z, V_x) = f(y, z, V_x) - f_{rot}(y, z, V_x) \quad (22)$$

as a measure of the amount of flux density associated with in-fall. Maps of F_{rot} and F_{fall} are displayed in Figure 12. The map of F_{rot} reveals the shape of the rotating CSE in the northern and southern hemispheres and F_{fall} , much smaller than F_{rot} , displays a clear enhancement of the in-falling flux along the diagonals of the map, in conformity with what is expected from accretion onto a flared disk. When swapping the y and z axes, the present situation is reminiscent of the Red Rectangle, the difference being that here rotation and in-fall combine everywhere while in the Red Rectangle case rotation and expansion are confined to different stellar latitudes. As in the Red Rectangle case, the effective emissivity can be calculated in space by solving the

relevant integral equation and the kinematics can be estimated assuming power law dependences of the rotation and in-fall velocities on r . A significant difference between protostars and evolved stars is that the former are embedded from the beginning into dense clouds from which they build their CSE, while the latter build their CSE from their own atmosphere; as a result the observation of protostar CSEs is subject to absorption complications that are absent from the observations of the CSEs of evolved stars. This is the case here where the Doppler velocities nearing the star systemic velocity are completely obscured. A detailed analysis of the consequences (Tuan-Anh et al. 2016) is beyond the scope of the present sub-section, the only purpose of which is to illustrate the very strong similarities between the studies of expanding CSEs of evolved stars and in-falling CSEs of protostars.

3.6 Multi-line observations

Many observations are not limited to a single molecular line, but often include flux densities associated with two or more different lines of a same molecule, for example two rotation lines of carbon dioxide. In such cases, very precious information is carried by the ratio of the measured flux densities. In making such a ratio, the gas density drops out and the emission probabilities are well known: if absorption can be neglected, the ratio of the flux densities is a direct measure of the relative population of the emitting quantum states, namely a direct measure of temperature. In many cases, the distance from the star is large enough for absorption to be small, but in any case the study of the line ratio provides very important information: it measures the temperature when absorption can be neglected and when the gas is in thermal equilibrium and has been in such a state for a long time, but if such hypotheses are not valid, it carries information about the importance and nature of their violation. Making good use of multi-line observations should not be limited to mapping the flux ratio measured in each pixel: in principle, the comparison between the observed lines can – and should – be extended to any other quantity that has been used in the analysis.

3.7 Asymmetries

In practice, real stars are often very far from obeying the axial symmetry assumed in the present article. A much more lumpy landscape is often to be expected. As a result, two different issues need to be considered: one is to which extent does this impact on the value and interest of a description that assumes axisymmetry, or even central symmetry; the other is to which extent deviations from the model can be simply described. While the answer to such questions is bound to carry some subjectivity, an essential preliminary consideration is to evaluate quantitatively the importance of the observed deviations.

Independently from any model, deviations from central symmetry can directly be evaluated from the asymmetry parameter

$$A_{\text{cntr}}(y, z, V_x) = \frac{f(y, z, V_x) - f(-y, -z, -V_x)}{f(y, z, V_x) + f(-y, -z, -V_x)} \quad (23)$$

Sky maps and P-V diagrams of this quantity tell both the importance and the nature of the observed deviations: they may be distributed more or less randomly in y , z and V_x or be concentrated in well-defined lumps. A systematic study of this asymmetry is an important complement to the studies described in the previous sections.

Revealing deviations from rotation invariance about the star axis cannot be done so directly. Partial information is contained in the symmetry – or lack of – about the z axis (or z' axis if ψ differs from 0) but extracting the full information requires a detailed analysis of the dependence of χ^2 on the star longitude (which is known in the model but unknown in the data). The outstanding quality of ALMA data allows for evaluating such a χ^2 much more reliably than was previously possible. Ideally, if the quality of the data would allow for a reliable evaluation of measurement uncertainties one could work in the uv plane and evaluate the degree of confidence attached to the fits and the uncertainties and cor-

relation coefficients attached to each of the model parameters in units of standard deviations. In general, however, one is far from such a situation. Even under ideal conditions, a significant lumpiness of the observed fluxes usually prevents a very faithful description, the model being at best a crude approximation of reality. As a result, the best fit values of χ^2 significantly exceed the number of degrees of freedom and one must rely on subjective arguments to obtain a sensible evaluation of the uncertainties attached to each of the model parameters.

4 SUMMARY AND CONCLUSION

The aim of the present work is to help constructing 3-D models of the CSE of axisymmetric radio sources, essentially evolved stars or protostars. The accent is on the kinematics, central to the astrophysics of AGB stars, more than on the morphology, for which exists an abundant literature, in particular in the domain of the deprojection of optical images of Planetary Nebulae (Steffen et al. 2011; Wenger et al. 2013, and references therein). It does not have the pretension to give recipes, not even strict guidelines, but simply to illustrate possibly more quantitative approaches to data analysis than often used in the current literature. Each star is a particular case: before starting modelling its CSE, one must first take into account the information available, optical, infrared or radio, and the physics considerations that are of relevance. In the present section, we summarize the results obtained in the preceding sections.

A number of preliminary points should be systematically examined before undertaking any modelling: they imply having a first close look at the data without requiring the help of a model. In particular the sky maps of $RF(y, z)$, of $\langle V_x \rangle$ and of $\langle |V_x| \rangle$ and their projections on the R and ϕ axes provide essential information. In addition to obtaining a global evaluation of the steepness of the decrease with r of the effective emissivity, one learns from them to which extent central symmetry is obeyed; whether there is any evidence for the effective emissivity to depart from spherical symmetry; whether axial symmetry is revealed on the $\langle V_x \rangle$ map; whether there is evidence for significant velocity gradients.

In a spirit of minimizing qualitative arguments and quantifying as much as possible the results of the analysis, use should be made of simple quantities that carry important information. Examples have been given, such as χ_ψ^2 and $A(\phi)$, which may help the evaluations of the orientation of the star axis in space and of the relative contributions of expansion along the star axis and rotation about it. They are not unique, other indicators and discriminators may be found better adapted to such and such a particular case.

Particular attention must be given to correlations between model parameters, such as between the inclination of the star axis on the line of sight, θ , and the elongation of the effective emissivity and/or wind velocity distribution along the star axis. If a χ^2 minimization method is used to adjust the model parameters, one should look at the dependence of χ^2 on θ , leaving all other parameters free to vary.

As well known from the practice of such studies, P-V diagrams carry very precious information. However, we have argued that using polar rather than Cartesian coordinates in the sky plane is often better suited to making the best

of them. In particular, the φ vs V_x diagrams have the advantage of being simply translated along the φ axis when ψ is varied, a useful feature when ψ is not known with precision, and their symmetry properties tell about the relative purity – or lack of – of expansion vs rotation. One must keep in mind that when expansion and rotation contribute significantly to the wind velocity in a same region of space, causing spiralling, the determination of the star axis is difficult. However, when expansion and rotation contribute significantly in different regions of space, this comment does not apply and their contributions to the P-V diagrams are simply superimposed.

The above arguments, as important as they may be, are not sufficient to construct a model. Physics considerations must also be taken in due account. While a precise hydrodynamic description is well beyond the scope of the present considerations, some of its most obvious features must be kept in mind when deciding on the form given to the effective emissivity and velocities. In particular the validity of the stationarity hypothesis needs to be critically discussed.

The concrete examples that have been given as illustrations of the above arguments have contributed new results to earlier analyses of the CO emission of the CSE of AGB stars. The study of RS Cnc has given an opportunity to comment on the hypothesis of stationarity of the wind regime and on a possible rotation of the equatorial volume about the star axis. In both cases, limits have been given to their possible contributions. In the case of EP Aqr, a picture has been drawn that unifies the presentation of the two models that had been proposed earlier, one with isotropic but r -dependent winds, the other with a bipolar outflow. Evidence has been given in favour of the latter. Results obtained in the case of the post-AGB Red Rectangle have been briefly recalled. Using Mira Ceti as an example, we have commented about the value of constructing, at least locally, a 3-D representation under the hypothesis of radial expansion at constant velocity. Such a representation is particularly useful to visualise the topology of the effective emissivity and reveal the presence of possible detached arcs, cavities, or isolated lumps. Finally, the example of a protostar, L1527, has been used to underline very strong similarities between the expanding CSEs of evolved stars and the in-falling CSEs of protostars.

ACKNOWLEDGEMENTS

We are deeply indebted to the anonymous referee for many comments and suggestions that helped considerably improving the quality of the manuscript. We are very grateful to the ALMA partnership, who are making their data available to the public after a one year period of exclusive property, an initiative that means invaluable support and encouragement for Vietnamese astrophysics. We particularly acknowledge friendly and patient support from the staff of the ALMA Helpdesk. This paper makes use of the following ALMA data: ADS/JAO.ALMA# 2011.0.00223.S, 2012.1.00524.S, 2013.1.00047.S, 2012.1.00647.S. ALMA is a partnership of ESO (representing its member states), NSF (USA) and NINS (Japan), together with NRC (Canada), NSC and ASIAA (Taiwan), and KASI (Republic of Korea), in cooperation with the Republic of Chile. The Joint

ALMA Observatory is operated by ESO, AUI/NRAO and NAOJ. The paper makes also use of observations carried out with the IRAM Plateau de Bure Interferometer and the IRAM 30-m telescope. IRAM is supported by INSU/CNRS (France), MPG (Germany) and IGN (Spain). We express our deepest gratitude to Professors Anne Dutrey, Stephane Guilloteau and Thibaut Le Bertre for the support, the interest in our work, and for very useful comments on the present manuscript. Financial support is acknowledged from VNSC/VAST, the NAFOSTED funding agency under grant number 103.99-2015.39, the World Laboratory, the Odon Vallet Foundation and the Rencontres du Viet Nam.

REFERENCES

- Decin, L., et al. 2015, *A&A*, 574, A5
 Hoai, D. T., et al. 2014, *A&A*, 565, A54
 Ihrke, I., Kutulakos, K., Lensch, H., Magnor, M. & Heidrich, W. 2008, *Proc. Eurographics EG '08 Annex*, pp. 87-108
 Leahy, D.A. 1991, *A&A*, 247, 584
 Lintu, A., Lensch, H.P.A., Magnor, M., El-Abed, S. & Seidel, H.-P. 2007, *Proc. IEEE/EG Int'l Symp. Volume Graphics*, Hege & Machiraju eds., 9
 Magnor, M., Kindlmann, G., Hansen, C. & Duric, N. 2004, *Proc. IEEE Visualization Conf.*, 83
 Magnor, M., Kindlmann, G., Hansen, C. & N. Duric, N. 2005, *IEEE Trans. Visualization and Computer Graphics*, 11/5, 485
 Nhung, P. T., et al. 2015a, *RAA*, 15, 5
 Nhung, P. T., et al. 2015b, *A&A*, 583, A64
 Ohashi, N., et al., 2014, *ApJ*, 796, 131
 Palmer, P.L. 1994, *MNRAS*, 266, 697
 Sabbadin, F. 1984, *MNRAS*, 210, 341
 Sabbadin, F., Cappellaro, E., Benetti, S. et al. 2000, *A&A*, 355
 Steffen, W., Koning, N., Wenger, S., Morisset, C. & Magnor, M. 2011, *IEEE Transactions on Visualization & Computer Graphics*, 17/4, 454
 Tobin, J.J., et al. 2012, *Nature*, 492/7427, 83
 Tuan-Anh, P., et al. 2015, *RAA*, Vol.15, No.12, 2213
 Tuan-Anh, P., et al. 2016, submitted to *MNRAS*, arXiv:1604.03801
 Wenger, S., Lorenz, D. & Magnor, M. 2013, *Computer Graphics Forum (Proc. of Pacific Graphics PG)*, 32/7, 93
 Winters, J. M., et al. 2007, *A&A*, 475, 559

APPENDIX A:

A1 Transformation relations between space and star coordinates

The star axis projects on z' , the transformed of z , on the sky (y, z) plane. In (x, y, z) coordinates, the star axis is a vector $(\cos \theta, \sin \theta \sin \psi, \sin \theta \cos \psi)$. For $\psi = 0$, the star axis projects on z on the sky plane, for $\theta = 0$ it is along x . The (x, y, z) to (ξ, η, ζ) transformation relations read:

$$\begin{aligned}\xi &= x \cos \theta + z \sin \theta \cos \psi - y \sin \theta \sin \psi \\ \eta &= z \sin \psi + y \cos \psi \\ \zeta &= -x \sin \theta + z \cos \theta \cos \psi - y \cos \theta \sin \psi\end{aligned}\tag{A1}$$

We define $r = \sqrt{x^2 + y^2 + z^2}$ and $R = \sqrt{y^2 + z^2}$, $\partial r / \partial x = x/r$ and write $y = R \cos \varphi$ and $z = R \sin \varphi$. A point in the star frame having latitude α (positive along ξ) and longitude ω is defined as $(\xi, \eta, \zeta) = r(\sin \alpha, \cos \alpha \cos \omega, \cos \alpha \sin \omega)$

with $-90^\circ < \alpha < 90^\circ$ and $-180^\circ < \omega < 180^\circ$. On the equator the zero of longitude ($\omega = 0$) is along $\eta = y'$.

Hence the transformation relations between (x, y, z) and (r, α, ω) read:

$$\begin{aligned} x &= r(\sin \alpha \cos \theta - \cos \alpha \sin \omega \sin \theta) \\ R \cos(\varphi - \psi) &= r \cos \alpha \cos \omega \\ R \sin(\varphi - \psi) &= r(\sin \alpha \sin \theta + \cos \alpha \sin \omega \cos \theta) \\ \omega &= \text{atan}\left[-\frac{x}{R} \sin \theta + \sin(\varphi - \psi) \cos \theta, \cos(\varphi - \psi)\right] \\ \alpha &= \text{asin}\left\{\left[x \cos \theta + R \sin(\varphi - \psi) \sin \theta\right] / \sqrt{x^2 + R^2}\right\} \\ r &= \sqrt{R^2 + x^2} \end{aligned} \quad (\text{A2})$$

Setting $\psi = 0$, a point $(\xi, \eta, \zeta) = (b, a \times \cos \omega, a \times \sin \omega)$, with a and b constant, projects on (y, z) in the sky plane. In the meridian plane of the star, it is a fixed point at $(a = r \cos \alpha, b = r \sin \alpha)$. In the sky plane

$$\left(\frac{y}{a}\right)^2 + \left(\frac{z - b \sin \theta}{a \times \cos \theta}\right)^2 = 1 \text{ and } a^2 - \left(\frac{z - b \sin \theta}{\cos \theta}\right)^2 = y^2 \quad (\text{A3})$$

Namely pixel (y, z) spans an hyperbola in the meridian plane of the star, while the point (a, b) spans an ellipse in the sky plane (Figure A1).

A2 Effective emissivity, wind velocity and their symmetries

Under the hypothesis of rotation invariance about the star axis, V_{rad} , V_{ax} and V_{rot} are functions of r and $\sin \alpha$ exclusively, independent of ω . Moreover, under the additional hypothesis of central symmetry, or equivalently of reflexion symmetry about the equatorial plane, V_{rad} and V_{rot} are even functions and V_{ax} an odd function of $\sin \alpha$. It is useful to define two symmetry operations: S_1 changing x in $-x$ and z in $-z$ but leaving y invariant and S_2 changing y in $-y$ but leaving x and z invariant. Table A1 summarizes symmetry properties of several quantities assuming rotational invariance about the star axis, central symmetry (or equivalently north-south symmetry with respect to the equator of the star) and $\psi = 0$. One may then rewrite the Doppler velocity as the sum of an expansion and a rotation components: $V_x = V_{x1} + V_{x2}$ with

$$\begin{aligned} V_{x1} &= (x/r)V_{\text{rad}} + \cos \theta V_{\text{ax}} \\ V_{x2} &= -\frac{R \cos(\varphi - \psi) \sin \theta}{r \cos \alpha} V_{\text{rot}} \end{aligned} \quad (\text{A4})$$

One sees from Table A1 that, for $\psi = 0$, V_{x1} is odd under S_1 and even under S_2 while V_{x2} is even under S_1 and odd under S_2 . However, when the value of ψ differs from zero, this is no longer true and maps of $\langle V_x \rangle$, $\langle V_x^2 \rangle$ or, for that matter, any other moment, do not reveal the position of the star axis: their symmetry properties depend on both the value of ψ and the relative importance of rotation and expansion.

A3 P-V diagrams

Setting $\psi = 0$, from the coordinate transformation relations between the star frame and the sky frame we obtain an important relation (Figure A2) between the star latitude α and x ,

$$r \sin \alpha = x \cos \theta + z \sin \theta \quad (\text{A5})$$

Table A1. Symmetry properties of several quantities under transformations S_1 and S_2 for $\psi = 0$ under the hypothesis of rotational invariance and central symmetry in the star frame.

	S_1	S_2	$S_1 \times S_2$
x	$-x$	x	$-x$
y	y	$-y$	$-y$
z	$-z$	z	$-z$
r	r	r	r
R	R	R	R
φ	$-\varphi$	$180^\circ - \varphi$	$180^\circ + \varphi$
α	$-\alpha$	α	$-\alpha$
ρ	ρ	ρ	ρ
V_{rad}	V_{rad}	V_{rad}	V_{rad}
V_{ax}	$-V_{\text{ax}}$	V_{ax}	$-V_{\text{ax}}$
V_{rot}	V_{rot}	V_{rot}	V_{rot}
V_{x1}	$-V_{x1}$	V_{x1}	$-V_{x1}$
V_{x2}	V_{x2}	$-V_{x2}$	$-V_{x2}$

For a given pixel, once we know x , we also know $r = \sqrt{x^2 + R^2}$ and α from the above relation: we can calculate the effective density and the gas velocity, and therefore the flux density $f(y, z, V_x) = \rho(x, y, z) dx/dV_x$. The dependence of the Doppler velocity on x is given by the relation $rV_x = xV_{\text{rad}} - y \sin \theta (\cos \alpha)^{-1} V_{\text{rot}}$ where V_{ax} has been set to zero.

Figure A2 displays a number of interesting features that are worth a mention. When $x \rightarrow -\infty$, $\sin \alpha \rightarrow -\cos \theta$; then, for $\sin \varphi > 0$, when x increases, so does $\sin \alpha$ until it reaches 0 for $u = -\sin \varphi \tan \theta$. Then, it keeps increasing and crosses the value $\cos \theta$ when $u = (\cos 2\theta + \sin^2 \theta \cos^2 \varphi) / (\sin 2\theta \sin \varphi)$. For $u = \sin \varphi / \tan \theta$, it reaches its maximum, $\sin \varphi / \sqrt{1 - \cos^2 \theta \cos^2 \varphi}$. In particular, when $\sin \varphi = \pm 1$ (z axis) it reaches the poles ($\sin \alpha = \pm 1$) at $u = \pm 1 / \tan \theta$. It then decreases slowly and for $x \rightarrow +\infty$, $\sin \alpha \rightarrow \cos \theta$. For $\theta = 0$, $\sin \alpha = u / \sqrt{1 + u^2}$ is independent of φ . For $\theta = 90^\circ$, $\sin \alpha = \sin \varphi / \sqrt{1 + u^2}$. For $\theta = 90^\circ$, $\sin \alpha = (u + \sin \varphi) / \sqrt{2(1 + u^2)}$. For $u = 0$, $\sin \alpha = \sin \varphi \sin \theta$. For $\sin \varphi = 0$, $\sin \alpha = u \cos \theta / \sqrt{1 + u^2}$ and for $\sin \varphi = \pm 1$, $\sin \alpha = (u \cos \theta \pm \sin \theta) / \sqrt{1 + u^2}$.

A4 Velocity spectra

In the case of pure rotation, setting $V_{\text{rot}} = V_0 \cos \alpha$, the spectral distribution takes a particularly simple form that illustrates well what happens:

$$dN/dV_x = r^2 R^{-1} \rho(r) [(\cos \varphi \sin \theta V_0)^2 - V_x^2]^{-1/2} \quad (\text{A6})$$

Namely the spectral distribution dN/dV_x increases from its value at $V_x = 0$ to infinity at the value $V_{\text{max}} = \cos \varphi \sin \theta V_0$, with

$$dN/dV_x \sim (V_{\text{max}}^2 - V_x^2)^{-1/2} \sim (2V_{\text{max}})^{-1/2} (V_{\text{max}} - V_x)^{-1/2} \quad (\text{A7})$$

For case A, the same qualitative behaviour is obtained: the main difference is that V_{rot} being now smaller in the equatorial region, the amplitude of the φ oscillations is also smaller. Finally, in case B, one is either inside the cone, in which case $V_{\text{rot}} = 0$, or outside, in which case $V_{\text{rot}} = V_0$ and

$$V_x = -\frac{R \cos \varphi \sin \theta}{r \cos \alpha} V_0 \quad (\text{A8})$$

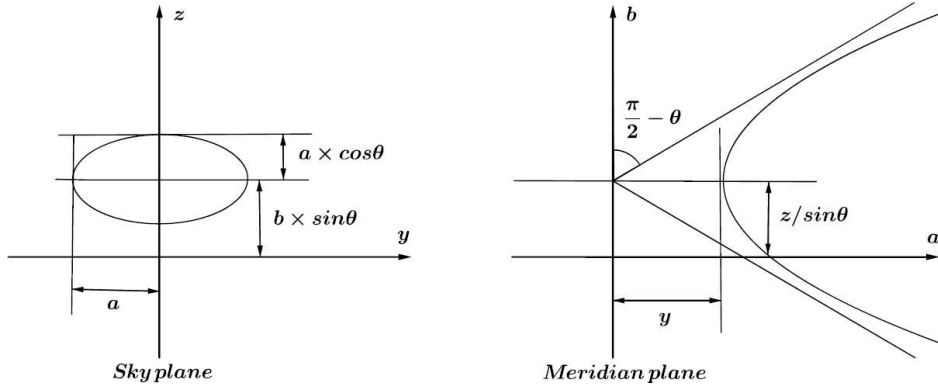


Figure A1. Left: Ellipse spanned in the sky plane by a fixed point (a, b) in the meridian plane. Right: hyperbola spanned in the meridian plane by a fixed point (y, z) in the sky plane.

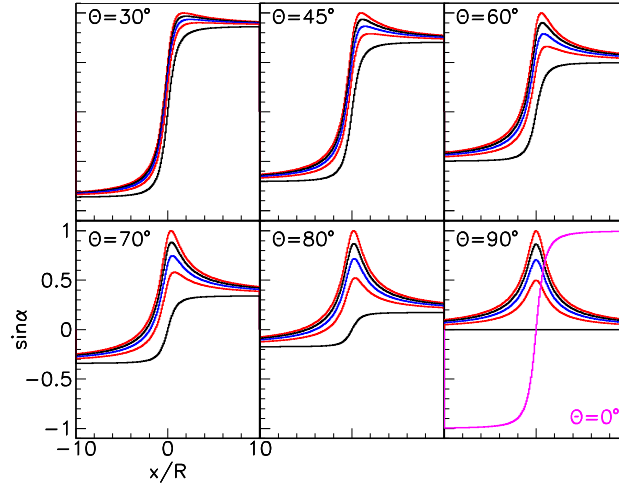


Figure A2. Distributions of $\sin \alpha = (u \cos \theta + \sin \phi \sin \theta) / \sqrt{1 + u^2}$ vs $u = x/R$. Each panel is for a fixed value of θ and in each panel, from down to up, ϕ varies as $0^\circ, 30^\circ, 45^\circ, 60^\circ$ and 90° . The last panel also includes the case $\theta = 0^\circ$ for which $\sin \alpha$ is independent from ϕ . Values of $\sin \alpha$ for $\sin \phi < 0$ are obtained by symmetry about the origin.

Outside the cone, $|V_x|$ reaches its maximal values V_0 for $|y| \sin \theta = r \cos \alpha$ and, as $\cos \alpha > 1/\sqrt{2}$, $R|\cos \phi| \sin \theta / r > 1/\sqrt{2}$, namely $r = R$ ($x = 0$) and $\cos^2 \phi \sin^2 \theta > 1/2$. Indeed, for pure rotation in case *B*, the ϕ oscillation of the extreme V_x values stays flat at maximum as long as $\cos \phi > 1/(\sqrt{2} \sin \theta)$. In particular, at $\theta = 90^\circ$, this happens over $\pm 45^\circ$ around $\phi = 0$ (*mod* 180°). A flat can only be seen if $\sin^2 \theta > 1/2$, meaning $\theta > 45^\circ$.

In the case of pure expansion, when the bipolar outflow is confined inside a cone of latitude α_0 , nothing changes inside the cone but the gas velocity, and therefore V_x , cancel outside the cone. The cone splits space in two regions, its interior and its exterior. On the sky plane, the limit is given by the relation $\cos \phi_{lim} = \tan \beta_0 / \tan \theta$ with $\beta_0 = 90^\circ - \alpha_0$ measuring the aperture of the cone. Note that any value of ϕ can be associated with a point outside the cone while only values of $\phi > \phi_{lim}$ can be associated with regions inside the cone. For $\phi > \phi_{lim}$ one has therefore $V_x = 0$. This happens only if $\cos \phi_{lim} < 1$, namely $\theta > \beta_0$. For smaller values of θ the interior of the cone covers the full sky plane. In general (Figure A3) the spectrum retains therefore the general form

$(V_0^2 - V_x^2)^{-3/2}$ but is confined to an interval smaller than the maximum interval $[-V_0, V_0]$.

A5 Evaluating the value of ψ

We define a quantity χ_ψ^2 as $\chi_\psi^2 = \chi_{\psi exp}^2 + \chi_{\psi rot}^2$ where

$$\begin{aligned} \chi_{\psi exp}^2 &= \sum_{exp} \{ [f(y, z, V_x) - f(y, 0, V_x)] \\ &\quad - [f(y, -z, -V_x) - f(y, 0, -V_x)] \}^2 / \Delta^2 \\ \chi_{\psi rot}^2 &= \sum_{rot} \{ [f(y, z, V_x) - f(0, z, V_x)] \\ &\quad - [f(-y, z, -V_x) - f(0, z, -V_x)] \}^2 / \Delta^2. \end{aligned} \quad (\text{A9})$$

The sum \sum_{exp} runs over pixels (y, z) located just a bit north of the y axis ($z > 0$ and small) and the sum \sum_{rot} over pixels (y, z) located just a bit east of the z axis ($y > 0$ and small). In addition, both sums run over the whole velocity spectrum. In each square bracket, the subtraction of the flux density measured on the axis, rotation on the y axis and expansion on the z axis, leaves us with the contribution

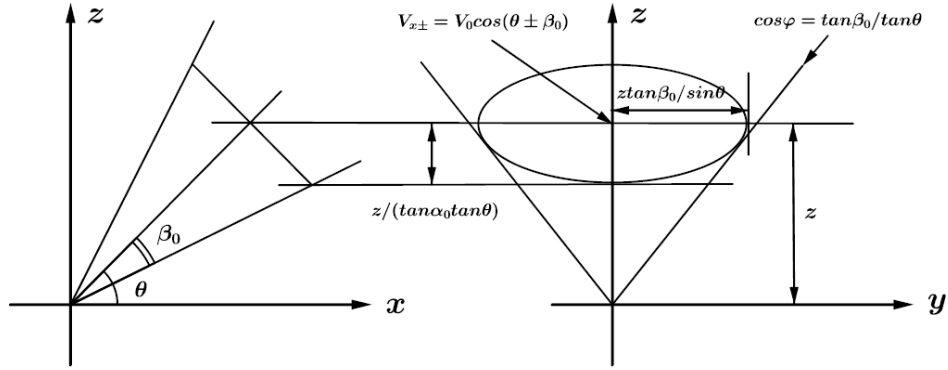


Figure A3. Conical bipolar outflow projected on the (x,z) plane (left) and the sky plane (right).

that changes sign under reflection about the axis, expansion about the y axis and rotation about the z axis. Therefore, if the z axis is the projection on the sky plane of the star axis, χ_ψ^2 nearly cancels when subtracting the two square brackets from each other. The value of ψ associated with the star axis is therefore expected to be that for which the quantity χ_ψ^2 , calculated for flux densities rotated by ψ about the origin on the sky map, reaches a minimum. The quantities Δ stand for the uncertainties attached to the measured flux densities. Here, we use for Δ the square root of the sum of the four flux densities appearing in the two square brackets of the relevant sum (which would be proper for purely statistical uncertainties). Figure A4 illustrates the difficulty of evaluating the proper value of ψ in the mixed case. It is drawn for $\theta = 45^\circ$ and for $V_{rad} = V_0 \cos q \sin^2 \alpha$ and $V_{rot} = V_0 \sin q \cos^2 \alpha$ for different values of q , namely of the relative importance of rotation vs expansion. The minimum is generally very shallow and in one case, $q = 20^\circ$, it is off by $\sim 5^\circ$. Better indicators than χ_ψ^2 may possibly be conceived, but they will always reveal the difficulty of measuring ψ when rotation and expansion compete for inclinations around $\theta = 45^\circ$.

A6 Telling rotation from expansion

Assuming $-V_{rot} > 0$ and writing $S_\pm(y,z) = \sum_\pm |V_x| f(y,z, V_x)$ where the sum extends over $\pm V_x > 0$, we have for pure rotation

$$\begin{aligned} S_+(y, \pm z) &= S_0; & S_-(y, \pm z) &= 0; \\ S_+(-y, \pm z) &= 0; & S_-(-y, \pm z) &= S_0 \end{aligned} \quad (\text{A10})$$

and for pure radial expansion

$$\begin{aligned} S_+(\pm y, z) &= S_1; & S_-(\pm y, z) &= S_2; \\ S_+(\pm y, -z) &= S_2; & S_-(\pm y, -z) &= S_1 \end{aligned} \quad (\text{A11})$$

Hence, writing $A_{as} = (S_+ - S_-)/(S_+ + S_-)$, $|A_{as}(y, \pm z)| = 1$ for pure rotation while for pure radial expansion $|A_{as}(\pm y, z)| = (|S_1 - S_2|)/(S_1 + S_2)$. Averaging over R , $A(\varphi) = \langle |A_{as}(R, \varphi)| \rangle = 1$ for pure rotation and $A(\varphi) = \langle (|S_1 - S_2|)/(S_1 + S_2) \rangle$ for pure expansion, which cancels for both $\theta = 90^\circ$ and $\theta = 0^\circ$ and is always smaller than unity. In the case of pure rotation, $A(\varphi) = 1$ independently from both φ and θ . The value of $A(\varphi)$ at $\varphi = 0^\circ$, $\varphi = 90^\circ$ or its integral over φ should therefore be good indicators of the relative importance of rotation over expansion. However, as soon as rotation is mixed

with some expansion, even when the latter is isotropic, $A(\varphi)$ starts departing from unity. Indeed, in the present article, for example in Figure 3, we usually considered expansion cancelling on the star equator. In reality, even in the presence of a clear bipolar outflow, some expansion may take place in the equatorial region. Moreover, the CSE may start its evolution with a small bipolar outflow and no global expansion or, on the contrary, with a small isotropic expansion. In the latter case, when the bipolar outflow starts to emerge, it is but a small perturbation to the isotropic expansion. We take this in consideration by writing $V_{rad} = V_0(1 + \lambda \sin^2 \alpha)$ and $V_{rot} = \mu V_0 \cos^2 \alpha$ (V_{rot} must cancel at the poles) and use an isotropic effective emissivity $\rho = \rho_0/r^2$. The parameters λ and μ measure the amount of respectively polar expansion and equatorial rotation that add to the isotropic expansion. We find that, to a good approximation, $A(90^\circ) = A(270^\circ) \sim A_{90} \sin 2\theta$ and $A(0^\circ) = A(180^\circ) \sim A_0 \sin \theta$ with A_{90} independent of μ (the $\cos \varphi$ factor in the contribution of rotation to V_x is the cause) and A_0 independent of λ . Both A_{90} and A_0 increase with respectively λ and μ as shown in Figure A5.

The above considerations suggest comparing the P-V diagrams of a $\lambda = 0$ case with a $\mu = 0$ case for a same value of θ . We choose $\theta = 45^\circ$ in order to maximize the effect of expansion and adjust μ and λ to have similar values of $A(\varphi)$. The associated P-V diagrams, shown in Figure A6, display small but significant differences. If, on the contrary, we adjust μ and λ to have similar effects on the P-V diagrams, we obtain much larger values of $A(\varphi)$ in the $\lambda = 0$ case (rotation) than in the $\mu = 0$ case (expansion). Figure A7 displays the Doppler velocity distributions obtained in this case on the positive y and z axes. The small differences illustrate the difficulty of telling expansion from rotation when they are small perturbations to a global isotropic expansion.

A7 Inclination θ of the star axis with respect to the line of sight

We first consider the dependence on θ of the integrated flux F . Its partial derivative with respect to φ , $F'_\varphi(R, \varphi)$, is expected to be an indicator of θ . Indeed, writing $\rho(r, \sin \alpha)$ the effective emissivity and using $\partial(\sin \alpha)/\partial \varphi = (R/r) \cos \varphi \sin \theta$, we obtain

$$F'_\varphi(R, \varphi) = R \cos \varphi \sin \theta \int \rho'_{\sin \alpha}(r, \sin \alpha) \frac{1}{r} dx, \quad (\text{A12})$$

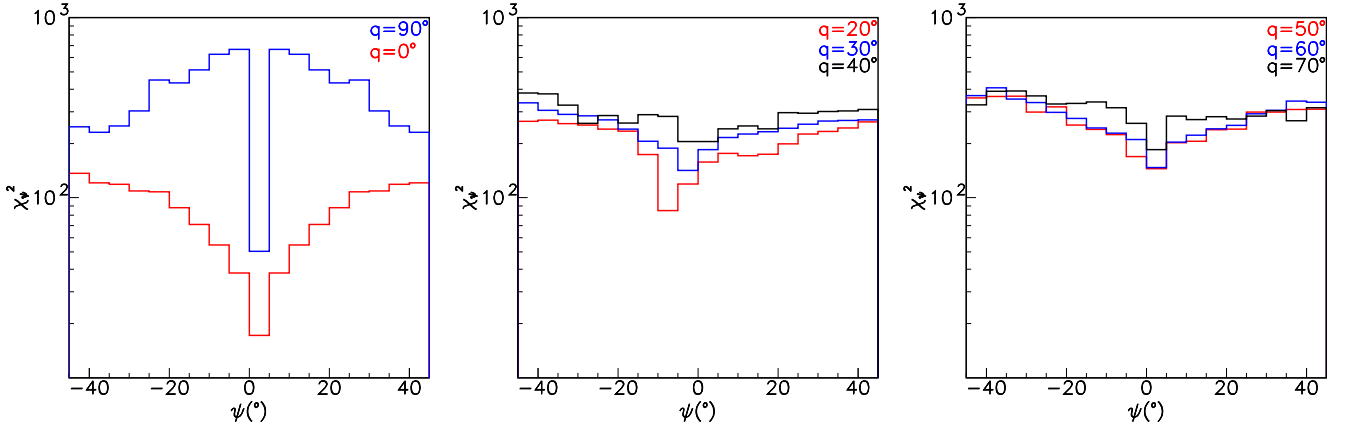


Figure A4. Distributions of χ^2_ψ as a function of ψ for case A and $\theta = 45^\circ$. The left panel is for pure expansion ($q = 0$, red) or pure rotation ($q = 90^\circ$, blue). The middle and right panels are for mixed expansion and rotation, their relative importance being measured by the angle q (see text) with values of 20° (red), 30° (blue) and 40° (black) in the middle panel, 50° (red), 60° (blue) and 70° (black) in the right panel. The projection of the star axis on the sky plane is at $\psi = 0$.

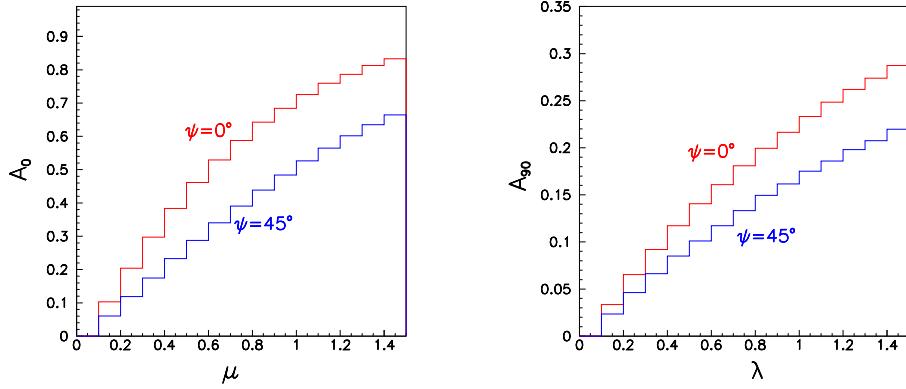


Figure A5. Dependence of A_0 on μ (left) and of A_{90} on λ (right) for $\psi = 0$ and $\psi = 45^\circ$ separately.

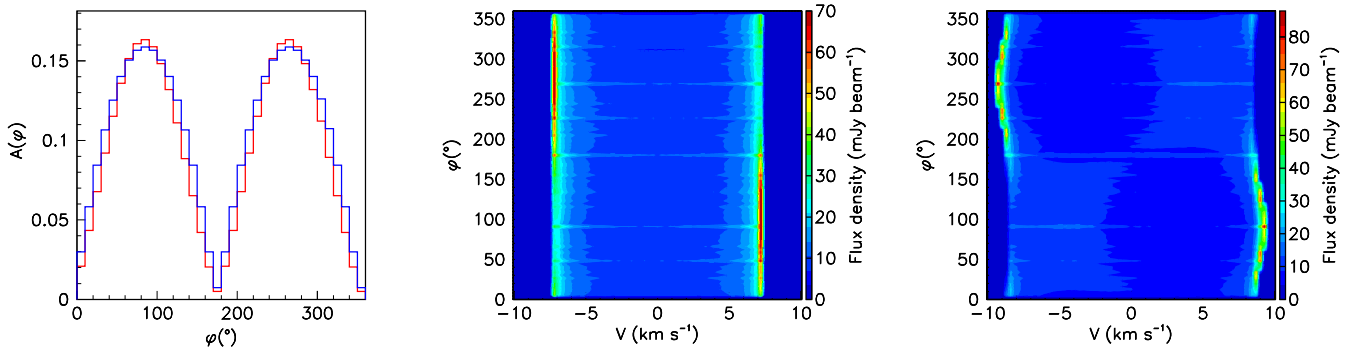


Figure A6. Comparison of the effect of a small rotation about the y axis (case 1, $\mu = 0.25$) with that of a bipolar expansion along the z axis producing the same value of $A(\phi)$ (case 2, $\lambda = 0.6$). Left panel: distributions of $A(\phi)$ for case 1 (blue) and case 2 (red). Middle and right panels: P-V diagrams for cases 1 and 2 respectively.

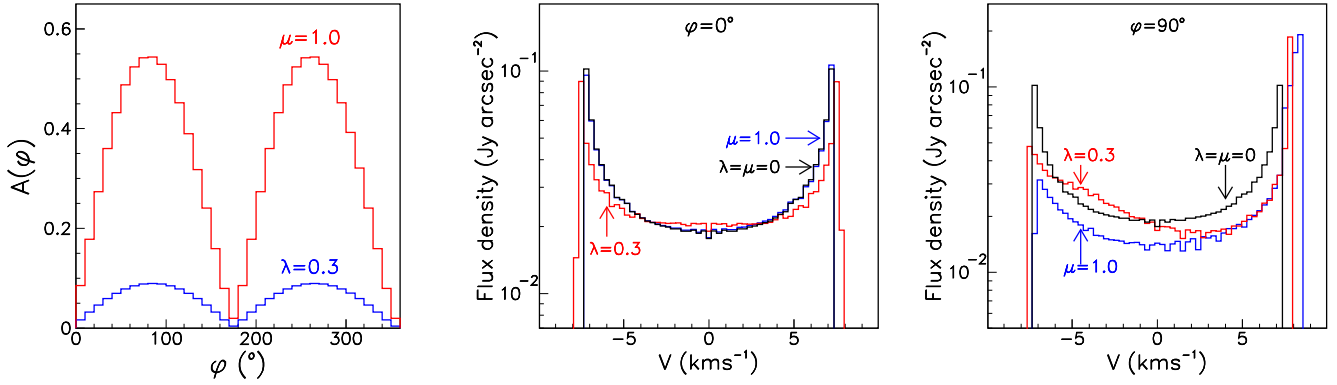


Figure A7. Comparison of the effect of a rotation about the y axis (case 1, $\mu = 1$) with that of a bipolar expansion along the z axis (case 2, $\lambda = 0.3$) producing similar effects on the P-V diagram. Left panel: distributions of $A(\varphi)$. Middle and right panels: Doppler velocity distributions obtained at $\varphi = 0^\circ$ (y axis) and $\varphi = 90^\circ$ (z axis) respectively. Black is for $\lambda = \mu = 0$, blue for case 1 and red for case 2.

namely

$$\sin \theta = F'_\varphi(R, \varphi) [R \cos \varphi \int \rho'_{\sin \alpha}(r, \sin \alpha) \frac{1}{r} dx]^{-1} \quad (\text{A13})$$

The dependence of F on φ is indeed an indicator of $\sin \theta$, however it requires the preliminary knowledge of the dependence of the effective emissivity on the star latitude, measured by $\rho'_{\sin \alpha}(r, \sin \alpha)$. It is not possible to evaluate θ independently from the elongation of the effective emissivity along the star axis. Indeed, modelling the effective emissivity as $\rho = \rho_0(1 + \lambda_\rho \sin^2 \alpha)r^{-2}$ (r measures in arcseconds), gives:

$$\begin{aligned} F'_\varphi(R, \varphi) &= R \cos \varphi \sin \theta \int 2\rho_0 \lambda_\rho \sin \alpha \frac{1}{r} dx \\ &= 2R\rho_0 \lambda_\rho \cos \varphi \sin \theta \int (x \cos \theta + z \sin \theta) \frac{1}{r^4} dx \end{aligned} \quad (\text{A14})$$

The x term in the parenthesis does not contribute to the integral and, writing $u = dx/R$,

$$\begin{aligned} F'_\varphi(R, \varphi) &= 2yz\rho_0 \lambda_\rho \sin^2 \theta \int \sqrt{u^2 + 1} du \\ &= \pi yz\rho_0 \lambda_\rho \sin^2 \theta \end{aligned} \quad (\text{A15})$$

Namely the dependence of the integrated flux on φ measures the product $\lambda_\rho \sin^2 \theta$: the inclination angle θ of the star axis on the line of sight cannot be measured from the map of integrated fluxes independently from the elongation λ_ρ of the effective emissivity along the star axis. Qualitatively, this result is expected to be always true. In the case of a spherically symmetric effective emissivity but axially symmetric wind velocity, a similar result applies. It is best seen in the case *B* of Section 2.3, which is particularly simple in this context. As seen in Figure A3, changing θ does not change the limits on the sky plane of the expansion cone as long as the ratio $\tan \beta_0 / \tan \theta$ is kept constant. Using this prescription, one may then readjust the values taken by the expansion and rotation velocities in order to minimize the changes experienced by the measured flux densities. On the axis of the cone, projected on the sky plane as the z axis, $V_x = V_0 \cos \theta$: keeping this product constant will limit the effect of changing θ to small variations of the limits of the velocity spectrum. Similarly, outside the cone, the Doppler velocity varies between 0 on the z axis ($y = 0$) to $V_0 \sin \theta$:

again, keeping this product constant will limit the effect of changing θ to small variations of the limits of the velocity spectrum.

In summary, when modelling the star with case *B* using five parameters ψ , θ , β , V_{exp} and V_{rot} (V_{exp} inside the cone and V_{rot} outside), very strong correlations affect the last four parameters leaving much arbitrariness in the value of θ . What we effectively measure are the ratio $\tan \beta_0 / \tan \theta$ and the products $V_{\text{exp}} \cos \theta$ and $V_{\text{rot}} \sin \theta$. Qualitatively, as for the effective emissivity, we measure the product of the inclination of the star axis on the line of sight by the elongation of the expansion cone. Another evidence for this ambiguity between inclination and elongation was obtained in Appendix A6 where $A(\varphi)$ was found to include a factor $\lambda \sin \theta$.

A8 Radial dependence of the CSE properties

For $\psi = 0$, in the case of a spherical effective emissivity, we may write

$$\rho(r, \sin \alpha) = \sum \rho_n r^{-n} \quad (\text{A16})$$

implying $F(R, \varphi) = \sum F_n(R, \varphi)$

with

$$F_n(R, \varphi) = \rho_n \int (x^2 + R^2)^{-\frac{n}{2}} dx = \rho_n R^{1-n} I_n \quad (\text{A17})$$

and

$$I_n = 2 \int (1 + u^2)^{-\frac{n}{2}} du$$

here, the integral runs from 0 to $+\infty$ and for $n = 2$, $I_2 = \pi$.

Hence

$$F'_R(R, \varphi) = \sum (1 - n) R^{-n} \rho_n I_n \quad (\text{A18})$$

the R -dependence of the integrated flux is simply related to the r -dependence of the effective emissivity. In particular, in case of a pure power law,

$$\rho(r, \sin \alpha) = \rho_n r^{-n} \quad (\text{A19})$$

$R^{n-1} F(R, \varphi)$ is a constant over the sky plane.

If central symmetry is obeyed, the mean value of V_x cancels. However, velocity gradients can be expected to show up on the expression of the square or absolute value of V_x .

In the case of radial expansion and assuming a pure power law dependence of the effective emissivity on r ,

$$\begin{aligned}
 I_n < |V_x| > &= R^{n-1} \int |x| V_{rad} r^{-n-1} dx \\
 &= 2 \int u V_{rad} (1+u^2)^{-\frac{1}{2}(n+1)} du \\
 &= \int V_{rad} v^{-\frac{1}{2}(n+1)} dv.
 \end{aligned} \tag{A20}$$

In the absence of gradient, $I_n < |V_x| > = \frac{1}{2}(n-1)V_{rad}$ is independent of R . In general, developing V_{rad} in powers of r , the R -dependence of $< |V_x| >$ depends simply on the r -dependence of the expansion velocity.

In the case of pure rotation, $V_x = y \sin \theta (r \cos \alpha)^{-1} V_{rot}$ and writing $V_{rot} = V_0 \cos \alpha r^{-k}$, a form making the enhancement of rotation in the equatorial region explicit, we obtain

$$\begin{aligned}
 I_n < |V_x| > &= y \sin \theta R^{n-1} \int \frac{1}{\cos \alpha} V_{rot} r^{-n-1} dx \\
 &= y \sin \theta V_0 R^{n-1} \int r^{-n-k-1} dx \\
 &= \cos \varphi \sin \theta V_0 R^{-k}.
 \end{aligned} \tag{A21}$$

The R -dependence of $< |V_x| >$ is the same as the r -dependence of V_{rot} .

This paper has been typeset from a \LaTeX file prepared by the author.